Journal of Power Sources 643 (2025) 237046

Contents lists available at ScienceDirect

Journal of Power Sources

journal homepage: www.elsevier.com/locate/jpowsour

Optimizing ZnSe microspheres through 2D MXene for asymmetric pseudocapacitive supercapacitors and efficient hydrogen production via water splitting☆

Inaam Ullah [a], Ayesha Irfan [a], Mai Li [a,*], Samira Saddique [b], Tiantian Yang [a], Hanxue Zhao [a], Nimra Irshad [a], Kaishuai Yang [c,***], Chunrui Wang [a,**], Paul K. Chu [d]

[a] College of Science, Donghua University, Shanghai 201620, China
[b] School of Materials Science and Engineering, University of Science and Technology Beijing, Beijing 100083, China
[c] School of Electronic and Information Engineering, Changshu Institute of Technology, Suzhou 215000, China
[d] Department of Physics, Department of Materials Science and Engineering, and Department of Biomedical Engineering, City, Tat Chee Avenue, Kowloon, Hong Kong

HIGHLIGHTS

- ZnSe microspheres with $Ti_3C_2T_x$ nanosheets boost electrochemical performance.
- ZnSe@$Ti_3C_2T_x$ achieves 1673.8 F g^{-1} and 98.81 % retention after 10,000 cycles.
- DFT simulations show strong stability and adsorption for ZnSe@$Ti_3C_2T_x$.
- AC//ZnSe@$Ti_3C_2T_x$-APSC device shows major improvements in energy storage.
- LSV tests confirm superior HER and OER performance of composite electrode.

GRAPHICAL ABSTRACT

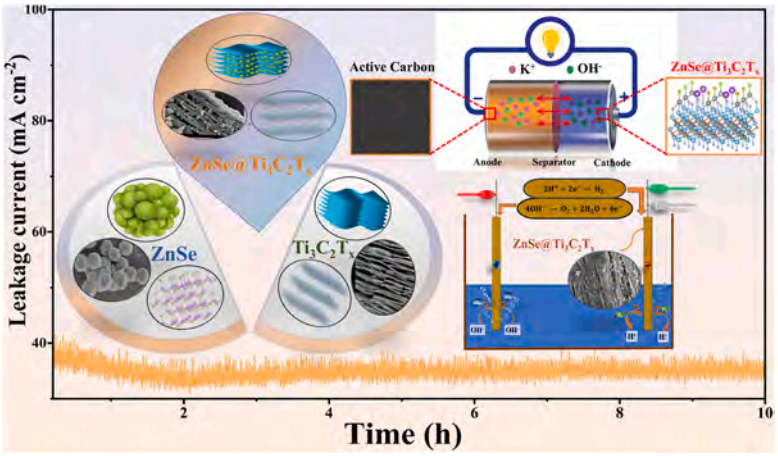

ARTICLE INFO

Keywords:
Electrochemical properties
Pseudocapacitive supercapacitor
$Ti_3C_2T_x$/MXene nanosheets
Composite electrode

ABSTRACT

In response to the increasing demand for sustainable energy, recent efforts have focused on developing novel composites with improved crystalline structures, chemical stability, and conductivity for electrochemical applications. Self-assembled zinc selenide (ZnSe) microspheres are synthesized by a simple hydrothermal process, and their electrochemical applications as a positive electrode/electrocatalyst in asymmetric pseudocapacitive supercapacitor (APSC) and water splitting are investigated. ZnSe is integrated into the two-dimensional (2D)

☆ Subject: Declaration of Interest Statement.

* Corresponding author.
** Corresponding author.
*** Corresponding author.
E-mail addresses: limai@dhu.edu.cn (M. Li), ksyang@cslg.edu.cn (K. Yang), crwang@dhu.edu.cn (C. Wang).

https://doi.org/10.1016/j.jpowsour.2025.237046
Received 26 August 2024; Received in revised form 26 December 2024; Accepted 10 April 2025
Available online 16 April 2025

Density-function theory (DFT)
Water splitting

$Ti_3C_2T_x$/MXene nanosheets that serve as a physical barrier to mitigate agglomeration, prevent side reactions of Zn, provide ZnSe with more sites and a steady Zn^{2+} supply, ultimately enhancing the electrochemical performance. Composite electrode demonstrates superior specific capacitance of 1673.8 F g^{-1} at 1 A g^{-1}, remarkable cyclic stability (98.81 % capacity retention over 10,000 cycles), and excellent pseudocapacitive performance of 88 % at 60 mV s^{-1}. Density functional theory (DFT) simulations displayed highest adsorption energy for ZnSe@$Ti_3C_2T_x$, showcasing stable structure and strong electron interaction. To demonstrate the commercial viability, active carbon (AC) is employed as the cathode to fabricate the AC//ZnSe@$Ti_3C_2T_x$-APSC device. In the water splitting assessment, ZnSe@$Ti_3C_2T_x$ shows the lowest Tafel slopes (~51.3 mV dec^{-1} for oxygen evolution reaction (OER) and ~36.9 mV dec^{-1} for hydrogen evolution reaction (HER)). This novel approach significantly advances the overall performance of APSC and water-splitting.

Dear Editor, I am writing to provide you with a Declaration of Interest Statement regarding the research we have conducted. As a member of Donghua University, I would like to solemnly declare that there are no financial or personal interests that could potentially bias the findings or interpretations presented in our research.

1. Introduction

Sustainable and efficient energy storage systems play an important role in the pursuit of green energy. Supercapacitors boasting rapid charging-discharging rates [1], high power densities, and long lifespans have emerged at the forefront of the development. However, the broader integration of supercapacitors is hampered by challenges such as limited capacity, constrained voltage range, and relatively small energy densities [2,3]. Researchers have focused on enhancing the surface activity and refining crystal structures to bolster the energy storage efficacy [4–6]. The properties of supercapacitors depend on materials such as metal selenides/oxides, conducting polymers, and carbon derivatives like activated carbon, carbon aerogel, and carbon nanofibers [7,8]. Transition metal selenides (TMSe) have emerged as promising electrode materials in energy conversion and storage due to ease of manufacturing, low cost, suitable bandgaps, safety, higher theoretical capacity, and high electrical conductivity compared to the metal oxide and sulfide counterparts [9,10]. The weak binding energy of TMSe enables efficient Faradaic discharging/charging [11–13]. In particular, zinc-based electrode materials have garnered significant attention in energy storage and conversion due to their high theoretical capacity (820 mAh g^{-1}), small ionic radius (0.74 Å) of Zn^{2+}, stability, reversibility, ductility, working potential (−0.762 V vs hydrogen electrode), eco-friendliness, and low cost [14–17]. Selenium exhibits superior metallic and intrinsic electrical characteristics compared to sulfur (5×10^{-1} S m^{-1}) and oxygen (1×10^{-1} S m^{-1}), with significantly higher electrical conductivity (10^{-3} S m^{-1}). The combination of selenium and zinc enables efficient electron and ion transport, resulting in enhanced electrochemical performance. For example, Yang et al. have demonstrated that ZnSe microspheres exhibit favorable charge transfer and a high reversible capacity of 433 mAh g^{-1} [18].

However, Zn electrodes face challenges such as NPs volume expansion, self-corrosion, reactive growth, passivation on the electrolyte/anode surface, and hydrogen evolution, which severely restrict their usage in energy storage applications [19–21]. Various strategies have been proposed to stabilize Zn-based electrodes/anodes [22,23]. 2D materials such as metal chalcogenides and metal carbides have attracted attention due to their exceptional properties [24–27]. The intricate nature of carbon-based materials necessitates the pursuit of innovative alternatives [28–30]. For example, T. Zhang et al. have synthesized the ZnSe@Carbon electrode with excellent cyclic stability and a capacity of 426.1 mAh g^{-1} after 3000 cycles at a current density of 5 A g^{-1} [31]. The implementation of MXene as a conductive additive in Zn-based electrochemical systems can confer notable benefits over carbon, including a large surface area, high conductivity, inherent metal vacancies, and hydrophilic nature, which synergistically can overcome the limitations plaguing energy storage [32–34]. These nanostructures exhibiting strong Vander Waal forces between MXene nanosheets help to mitigate aggregation and enhance the reaction kinetics [35]. However, pure MXene faces limitations in terms of energy density and reaction stability, but incorporating MXene into composite electrodes improves the energy density and alleviates the agglomeration of active materials [36–38]. Karkuzhali et al. have studied the incorporation of MXene into CoNi(O_x)Se revealing significant improvements such as a specific capacitance of 1782 F g^{-1}, 95 % capacity retention after 5000 cycles, and an energy density of 131.9 Wh kg^{-1} at a power density of 7.2 kW kg^{-1} [39]. The use of TMSe electrodes in energy storage is limited by self-agglomeration and side reactions, but 2D materials like $Ti_3C_2T_x$ are being explored to mitigate these issues and enhance ion diffusion. However, there is still a need for significant improvement, underscoring the importance of further enhancing the structural and morphological properties of $Ti_3C_2T_x$.

Electrochemical water splitting generates high-quality hydrogen (H_2) from water sources with varying pH levels (acidic, neutral, and basic) for clean energy applications [40,41]: $2H_2O(l) \rightarrow 2H_2(g) + O_2(g)$, with $\Delta E_o = 1.23$ V vs. RHE. However, the overpotential of 1.23 eV necessitates the use of electrocatalysts (237 kJ mol^{-1}) for the cathodic or anodic processes [42,43]. ZnSe is a promising candidate for water splitting on account of efficient visible light absorption, a narrow bandgap (2.7 eV), eco-friendly nature, and low cost [44]. However, ZnSe suffers from aggregation and potential side reactions of Zn, which can impact the oxygen evolution reaction (OER) and hydrogen evolution reaction (HER) activities, and $Ti_3C_2T_x$ has been proposed to overcome these drawbacks [45]. For example, M. Saquib et al. have synthesized NiMoSe/MXene@CC showcasing superior overpotential of 203 mV at a current density of 10 mA cm^{-2} and a Tafel slope of 45 mV dec^{-1} for HER as well as 320 mV with a Tafel slope of 189 mV dec^{-1} [46]. However, there is an urgent need to produce better composite materials with outstanding morphology and structure for high-performance energy storage devices and electrolysis.

Herein, the ZnSe@$Ti_3C_2T_x$ composite is synthesized by simple hydrothermal and solvothermal techniques to form the positive electrode, as shown in Fig. 1. Firstly, the agglomerated spherical ZnSe NPs are synthesized hydrothermally, and in order to mitigate agglomeration and increase the active sites, the Al layers are removed from Ti_3AlC_2 to generate more active sites. ZnSe is anchored to the $Ti_3C_2T_x$ nanosheets to form the ZnSe@$Ti_3C_2T_x$ nanocomposite. Systematic characterization reveals the excellent crystal structure and morphology and mitigated ZnSe agglomeration because of ample active sites and large area of the $Ti_3C_2T_x$ nanosheets together with limited side reactions of Zn. The capacity retention of ZnSe remains at 88.8 %, while ZnSe@$Ti_3C_2T_x$ shows a capacity retention of 98.81 % and a specific capacitance of 1673.8 F g^{-1} at 1 A g^{-1}. To demonstrate the applicability, the AC//ZnSe@-$Ti_3C_2T_x$-APSC with AC as the cathode shows cyclic stability of 91.92 % after 10,000 cycles, capacitance of 259.12 F g^{-1} at 1 A g^{-1}, and maximum specific energy density of 92.90 Wh kg^{-1} at a power density of about 803.3 W kg^{-1}. Remarkable improvements in the OER and HER activities are also observed from ZnSe@$Ti_3C_2T_x$ in water-splitting experiments.

The ZnSe, $Ti_3C_2T_x$, and ZnSe@$Ti_3C_2T_x$ composites were fabricated by hydrothermal and solvothermal techniques, as shown in Supporting Section S1. Fabricated materials were deposited onto pre-treated nickel

foam (NF) (Supporting Section S1.4.) to form the working electrodes illustrated by SEM images (Fig. S1). For this a mixture containing 0.5 ml of deionized water, 0.4 ml of isopropyl alcohol, 0.04 ml of Nafion, and 10 mg of the synthesized materials was prepared. This mixture was sonicated in an ice bath for 1 h and coated uniformly on pre-treated NF, followed by drying at 80 °C for 2 h.

In the three-electrode setup, $Hg/Hg_2Cl_2/KCl$ (potential of 0.238 V) was the reference electrode, a Pt wire served as the counter electrode, and the working electrode was ZnSe, $Ti_3C_2T_x$, or $ZnSe@Ti_3C_2T_x$. In the storage experiments, 2 M KOH was the electrolyte, but in water splitting only 1 M KOH solution was used. The CHI660E electrochemical workstation was employed to conduct cyclic voltammetry (CV), galvanostatic charging-discharging (GCD), electrochemical impedance spectroscopy (EIS) in the frequency range 0.1 Hz–1 MHz, linear sweep voltammetry (LSV) and chronoamperometry test (for 10 h).

In the APSC, the $ZnSe@Ti_3C_2T_x$ electrode was used as positive electrode, and the counter electrode consisted of a mixture of 80 % active materials, 10 % carbon black, (CB), and 10 % polyvinylidene fluoride (PVDF) as a binder mixed with a few drops of N-methyl-2-pyrrolidone (NMP). Stirring was performed for 24 h at moderate speed. This mixture was applied evenly onto the NF substrate and dried under vacuum at 70 °C for 24 h. The total mass of the electrode materials varied between 2.5 and 3.5 mg cm^{-2}. APSC coin cell was fabricated by integrating the positive electrode ($ZnSe@Ti_3C_2T_x$) and negative electrode (AC), parted by organic separator and filled with 7 M KOH aqueous electrolyte.

2. Results and discussion

The materials fabrication is illustrated in Fig. 1 Initially, agglomerated spherical ZnSe NPs are hydrothermally synthesized to ensure the formation of homogeneous and well-defined nanostructures. To mitigate agglomeration and increase the number of active sites, Al layers are removed from Ti_3AlC_2. Subsequently, an anchoring process is employed to insert the ZnSe NPs into the $Ti_3C_2T_x$ nanosheets to form the $ZnSe@Ti_3C_2T_x$ nanocomposite. Rigorous characterizations are carried out as deeply described in Supporting section S2.

SEM, TEM, and HR-TEM are performed to deeply investigate the morphology of synthesized materials. In Fig. 2a and (Fig. S2a), the ZnSe NPs self-assembled to form larger spherical microspheres during the synthesis process. Fig. 2b shows the multi-layered and flexible 2D $Ti_3C_2T_x$ sheets. HCl/LiF etching eliminates Al layers from Ti_3AlC_2 to increase the surface area and active sites (Figs. S3a and S3b). HR-TEM is employed to observe the ultrathin $Ti_3C_2T_x$ sheets (Fig. S3c). Fig. 2c and d displays that the ZnSe NPs occupy the active sites on the $Ti_3C_2T_x$ sheets to form the $ZnSe@Ti_3C_2T_x$ composite (Fig. S4a). $Ti_3C_2T_x$ mitigates the agglomeration of ZnSe during synthesis and facilitates direct integration. In Fig. 2e TEM image shows the uniform and dense ZnSe NPs (Fig. S2b). In Fig. 2f TEM image illustrates that ZnSe NPs are inserted into the ultrathin layer of $Ti_3C_2T_x$. A significant number of NPs with small diameters averaging 10–30 nm are observed (Fig. S4b). Fig. 2g shows HR-TEM image demonstrating two layers, one layer with a spacing of 0.326 nm corresponding to the (111) plane of ZnSe, which is surrounded by an ultrathin layer of $Ti_3C_2T_x$, while the other layer associated with $Ti_3C_2T_x$ nanosheets with a spacing of 1.16 nm corresponding the (002) plane. The inset reveals the SAED pattern illustrating polycrystalline NPs scattered throughout, with some blurry diffraction spots indicating spherical nanostructures, which are likely ZnSe NPs. Several diffraction rings related to (111), (220), and (311) indicate the pure crystal structure of ZnSe, and the ring corresponding to (002) suggests the presence of $Ti_3C_2T_x$ [47]. The calculated size of ZnSe NPs is between 10 and 30 nm demonstrated in Fig. 2h while the average calculated size of ZnSe is 22.04 nm, which is the most suitable for insertion into the $Ti_3C_2T_x$ nanosheets (Fig. 2i). Fig. 2(j-j7) shows the EDS mapping of the synthesized $ZnSe@Ti_3C_2T_x$ nanocomposite revealing Ti, C, Zn, and Se, while functional groups (F, Cl, and O) are also present, albeit at lower concentrations. Fig. 2k shows the concentrations determined by EDS and the ratio of Zn to Se is 3 to 1. The concentrations of the other major elements in $ZnSe@Ti_3C_2T_x$ are: Ti = 46.2 %, C = 15 %, Zn = 21.8 %, and Se = 7.4 %.

Fig. 3a presents the XRD spectra confirming the crystal phase in the as-synthesized MAX powder (Ti_3AlC_2), $Ti_3C_2T_x$, ZnSe, and $ZnSe@Ti_3C_2T_x$. The etching of the Al layers and the formation of $Ti_3C_2T_x$ sheets are validated by the 11° angle shift in the (002) peak and the disappearance of the prominent peak at 38° [48]. The XRD spectrum of the ZnSe microspheres exhibits peaks at 2θ = 27.26°, 45.4°, 53.8°, 66.1°, and 72.9°, corresponding to the (111), (311), (220), (400), and (331) planes, respectively (JCPDS card no. 37–1463). These results confirm the successful synthesis of ZnSe spherical microstructures. A slight shift in the ZnSe peak and decreased intensity are detected, indicating the incorporation of ZnSe NPs into the inner and outer surface sheets of the $Ti_3C_2T_x$ nanostructures.

Fig. 3b illustrates the relationship between the crystal size and full-width at half-maximum (FWHM) of the ZnSe NPs. The Debye Scherer equation, $D = k\lambda/\beta Cos\theta$, is used to determine the crystal size, displaying that the average size of the ZnSe NPs is between 10 and 30 nm. The small

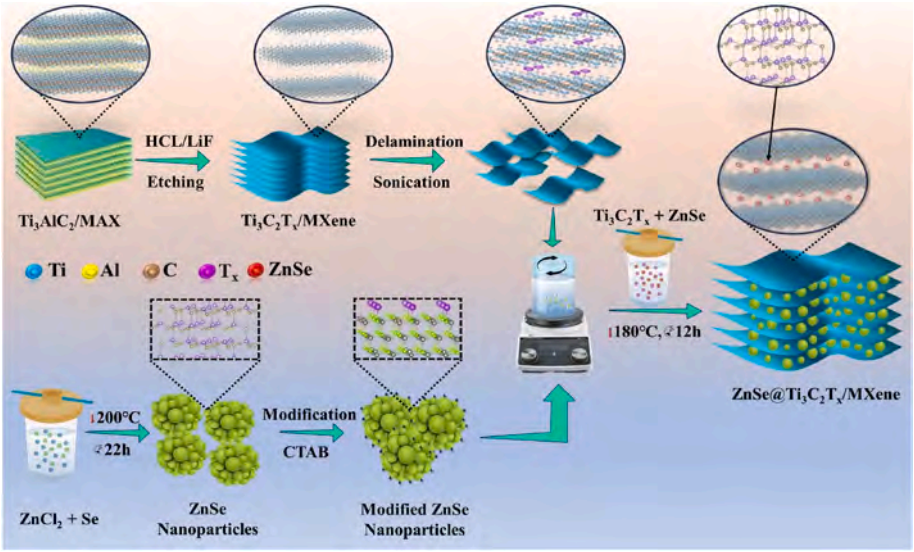

Fig. 1. Schematic illustration of the synthesis of agglomerated ZnSe microspheres, $Ti_3C_2T_x$/MXene nanosheets, and $ZnSe@Ti_3C_2T_x$/MXene nanocomposites.

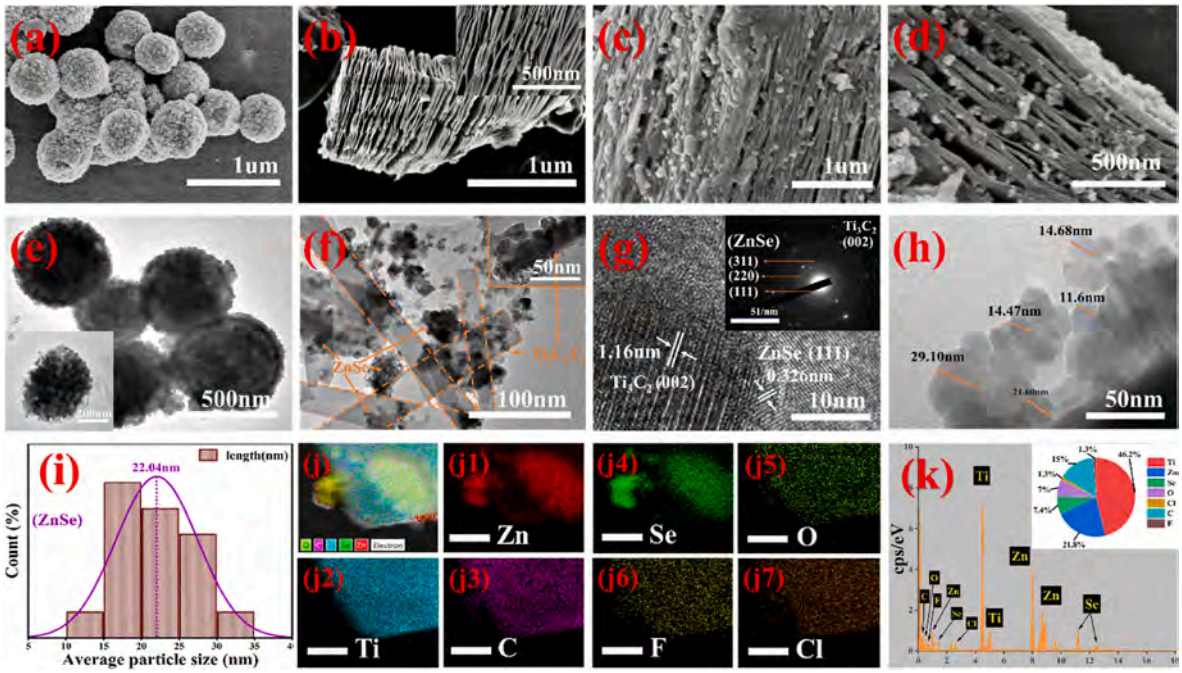

Fig. 2. SEM images of (a) ZnSe microspheres, (b) $Ti_3C_2T_x$ nanosheets, and (c–d) ZnSe@$Ti_3C_2T_x$ composite nanostructure; TEM image of (e) ZnSe; HR-TEM images of (f) ZnSe@$Ti_3C_2T_x$; (g) Polycrystalline nature of the nanocomposite with the inset displaying the SAEED pattern; (h) HR-TEM image of ZnSe@$Ti_3C_2T_x$; (i) Average particle size of ZnSe; (j-j7) EDS maps of ZnSe@$Ti_3C_2T_x$ with the scale bare of 250 nm; (k) Concentrations determined by EDS.

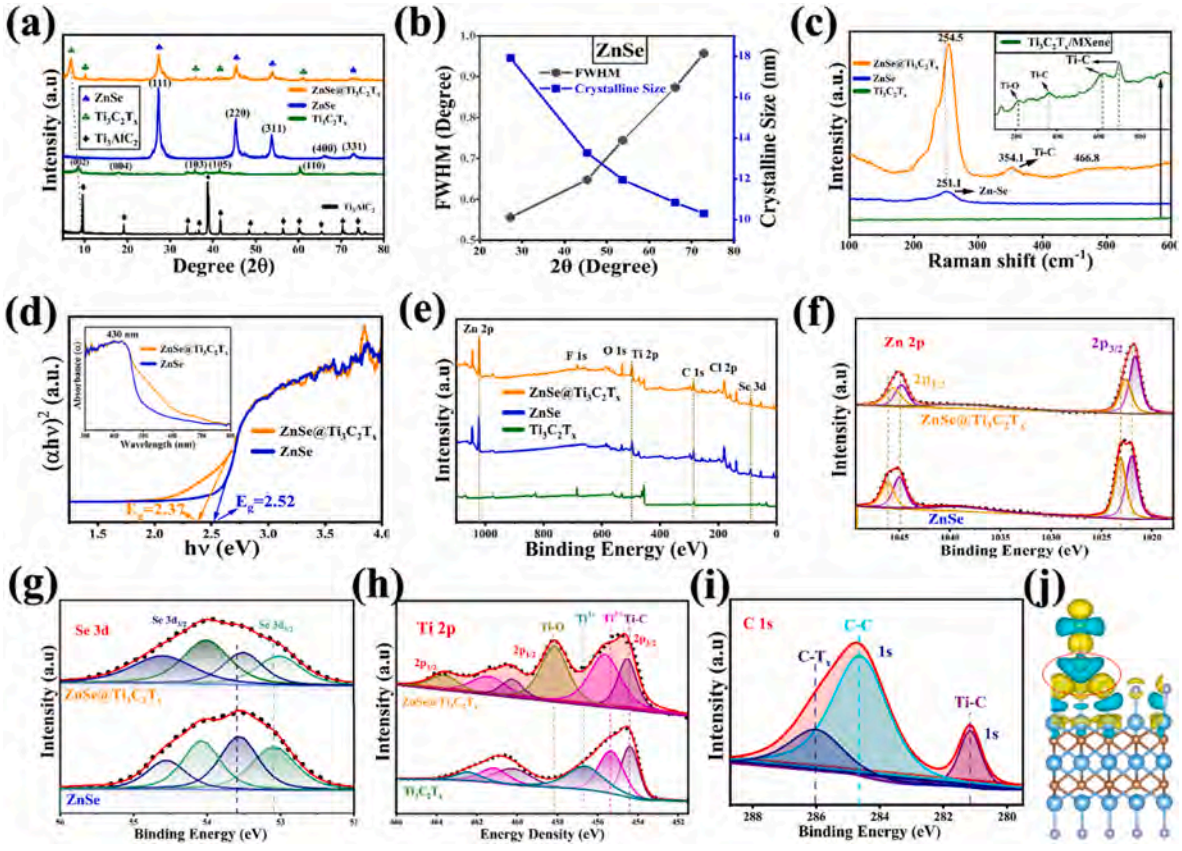

Fig. 3. (a) XRD patterns of Ti_3AlC_2, $Ti_3C_2T_x$, ZnSe, and ZnSe@$Ti_3C_2T_x$; (b) FWHM vs crystalline size of ZnSe NPs; (c) Raman spectra; (d) Bandgap and adsorption spectra; XPS spectra: (e) Full spectra (f) Zn 2*p*, (g) Se 3*d*, (h) Ti 2*p*, and (i) C 1*s*, (j) Charge difference analysis by CDD.

crystallites in the ZnSe@$Ti_3C_2T_x$ composite arise from reduced dislocation density and lattice strain, resulting in a larger surface area [49]. Fig. 3c shows Raman spectra of all synthesized materials. A peak with low intensity is observed at 701 cm^{-1} from Ti-C, and that at 251.1 cm^{-1} indicates the LO mode of ZnSe [50]. The peak at 254.5 cm^{-1} confirms the improved crystallinity and molecular bonding, with a peak shift from 251.1 cm^{-1} to 254.5 cm^{-1} for ZnSe NPs. Two minor peaks at 354.1 cm^{-1} and 466.8 cm^{-1} indicate Ti-C and O-Ti-O, indicating the reaction of $Ti_3C_2T_x$ with water during the synthesis process [51]. Fig. 3d shows the UV results and calculated bandgaps of ZnSe and ZnSe@$Ti_3C_2T_x$. The bandgap of ZnSe is determined to be 2.52 eV. The decrease in the bandgap is 0.15 eV indicating a smaller bandgap of 2.37 eV for ZnSe@$Ti_3C_2T_x$. The decrease in bandgap confirms the synergistic effect of composite material. The inset shows Adsorption edges in the range of 400–500 nm, with a sharp edge at 430 nm for ZnSe@$Ti_3C_2T_x$ [52].

The BET surface area analysis (Fig. S5) reveals that the ZnSe@-$Ti_3C_2T_x$ composite exhibits a significant increase in surface area (53.2 m^2/g) compared to pure ZnSe (21.5 m^2/g) and $Ti_3C_2T_x$ (30.14 m^2/g), indicating enhanced surface availability for electrochemical reactions. This increase in surface area is attributed to the synergistic effect between ZnSe and $Ti_3C_2T_x$, which provides more active sites and improved contact between the materials, contributing to the superior electrochemical performance.

XPS was employed to investigate the composition and chemical states of the $Ti_3C_2T_x$ and ZnSe@$Ti_3C_2T_x$ composites (Fig. 3e), where the characteristic peaks for Zn 2*p*, Se 3*d*, Ti 2*p*, and C 1*s* were observed. In addition, the presence of F, Cl, and O was also confirmed. The high-resolution Zn 2*p* spectrum Fig. 3f revealed two distinct peaks at 1022.0 eV and 1044.6 eV, corresponding to Zn $2p_{3/2}$ and Zn $2p_{1/2}$, respectively, which are characteristic of Zn^{2+} in ZnSe. In the composite, ZnSe@$Ti_3C_2T_x$, these peaks shifted slightly to 1021.17 eV and 1044.14 eV, indicating an interaction between Zn and the $Ti_3C_2T_x$ substrate, likely due to charge redistribution at the interface, which may suggest interfacial charge transfer between ZnSe and $Ti_3C_2T_x$. These shifts could be due to the strong coupling between ZnSe and the conductive $Ti_3C_2T_x$ sheets, affecting the electron density around Zn atoms. The Se 3*d* spectrum Fig. 3g shows two peaks at 54.1 eV and 55 eV, corresponding to Se $3d_{3/2}$ and Se $3d_{5/2}$, respectively, in ZnSe [53]. A slight shift in the Se binding energy was observed in the ZnSe@$Ti_3C_2T_x$ composite, indicating a reduction in binding energy, which further supports the occurrence of interfacial charge transfer between ZnSe and $Ti_3C_2T_x$. For Ti 2*p* Fig. 3h the spectrum of $Ti_3C_2T_x$ showed a Ti-C bond peak at 454.4 eV, corresponding to Ti-C bonding in $Ti_3C_2T_x$, which shifted to 454.64 eV in the ZnSe@$Ti_3C_2T_x$ composite. A similar shift was observed for the Ti^{2+} peak, which shifted from 455.36 eV in $Ti_3C_2T_x$ to 455.82 eV in the composite. Notably, the Ti^{3+} peak, present in pure $Ti_3C_2T_x$, vanished in the ZnSe@$Ti_3C_2T_x$ spectrum, suggesting that the oxidation state of Ti changed, likely due to the interaction between ZnSe and $Ti_3C_2T_x$. Additionally, a new peak at 458.42 eV corresponding to Ti-O bonding was observed in the composite, which was absent in the pure $Ti_3C_2T_x$ spectrum, suggesting slight oxidation of $Ti_3C_2T_x$ upon coupling with ZnSe. This Ti-O peak may also indicate the formation of an interface layer contributing to the enhanced electrochemical performance of the composite.

The surface contribution of C-C is shown in Fig. 3i. The peaks at 281.16, 284.65, and 288 eV stem from Ti-C, C-C, and C-F [54,55]. The presence of Ti-C and C-C shows strong bonding of $Ti_3C_2T_x$ nanosheets.

The charge density difference (CDD) analysis of the ZnSe@$Ti_3C_2T_x$ composite (Fig. 3j) provides key insights into the electron transfer dynamics between ZnSe and the $Ti_3C_2T_x$. In the CDD plot, cyan regions indicate a decrease in charge density, while yellow regions represent an increase in charge density. The visualization clearly shows that electrons have been transferred from ZnSe to $Ti_3C_2T_x$, confirming the strong interaction between these two materials.

To quantify this electron transfer, Bader charge analysis (BCA) was performed. The BCA calculation revealed that the total number of electrons associated with the Zn and Se atoms is reduced when ZnSe forms a composite with $Ti_3C_2T_x$. The electron transfer can be determined by subtracting the remaining charge from the total number of valence electrons in ZnSe. For Zn and Se: $(12 + 6) - (11.04 + 6.26) = 0.70$, This result indicates that approximately 0.7 electrons are transferred from ZnSe to $Ti_3C_2T_x$. This electron transfer facilitates improved charge mobility and conductivity in the composite, significantly enhancing the electrochemical performance in energy storage applications. The transfer of electrons from ZnSe to the conductive $Ti_3C_2T_x$ nanosheets supports the pseudocapacitive behavior observed, where the $Ti_3C_2T_x$ not only provides active sites but also acts as an efficient electron transport matrix, thereby improving the overall electrochemical performance of the composite electrode.

2.1. Electrochemical properties

The synthesized electrode materials undergo a rigorous electrochemical assessment to ascertain their suitability in energy storage applications (Supporting section S5). CV curves are acquired at scanning rates from 1 to 150 mV s^{-1}, while the potential is in the range of 0–0.6 V. Fig. 4a shows the comparison of the CVs of NF, $Ti_3C_2T_x$, ZnSe, and ZnSe@$Ti_3C_2T_x$ electrodes at a scanning rate of 10 mV s^{-1}. ZnSe@-$Ti_3C_2T_x$ outperforms the others as demonstrated by the largest CV area and highest current densities. Fig. 4b and c displays the CV results for ZnSe and ZnSe@$Ti_3C_2T_x$. The higher current densities indicate that ZnSe and ZnSe@$Ti_3C_2T_x$ have high-rate capability and low internal resistance. ZnSe@$Ti_3C_2T_x$ shows a significant increase in the CV area and reduced contact resistance. Significantly, the presence of redox peaks at high scanning rates indicates a dynamic interfacial response, characterized by reversible Faradaic reactions and electron transfer as evidencing the valence changes in Zn^{2+}. The CVs of NF and $Ti_3C_2T_x$ in (Figs. S6a–b) reveal inferior properties.

Fig. 4d shows the comparison of charging and discharging patterns of different electrodes at current density of 1 A g^{-1} in a potential window 0–0.6V. The voltage response observed in GCD curves were in complete accordance with the CV curves. Comparison shows ZnSe@$Ti_3C_2T_x$ electrode exhibits the longest discharging duration as compared to ZnSe and $Ti_3C_2T_x$. The longer discharge time is proposed to the interaction between the electrolyte and $Ti_3C_2T_x$ significantly influences ion mobility, thereby impeding ion diffusion within the electrolyte towards the active sites of ZnSe. In Fig. 4e and f, GCD curves display charging and discharging characteristics of ZnSe and ZnSe@$Ti_3C_2T_x$ for current densities from 1 to 20 A g^{-1}. Longer discharging times are observed at lower current densities, particularly at 1 A g^{-1} meanwhile high symmetry of the GCD curves show high Coulombic efficiency and excellent redox reaction reversibility. GCD curves of NF and $Ti_3C_2T_x$ are also demonstrated in Figs. S7(a–b) at various current densities. Fig. 4g shows the correlation between the current density and specific capacity for current densities spanning 1–20 A g^{-1}. The ZnSe@$Ti_3C_2T_x$ electrode, due to its enhanced structural integrity and dispersion, high electrical conductivity, and controlled ion diffusion, shows a longer charging/discharging time (for 1 cycle) of 1922.4 s, surpassing 959.7 s of the ZnSe electrode the same conditions. The durability and long-term stability of ZnSe, $Ti_3C_2T_x$, and ZnSe@$Ti_3C_2T_x$, are presented in Fig. 4h. ZnSe@$Ti_3C_2T_x$ displays outstanding cyclic stability with a capacity retention of 98.81 % after 10,000 cycles, surpassing ZnSe and $Ti_3C_2T_x$ with capacitance retentions of 88.8 % and 80.22 %, respectively.

EIS is employed to assess the kinetic behavior, including ion diffusion, ion conductivity, and resistance. The Nyquist plots in Fig. 4i reveal that ZnSe@$Ti_3C_2T_x$ has the smallest semicircle in the high-frequency region compared to pristine ZnSe and $Ti_3C_2T_x$. The calculated charge transfer resistances (R_{ct}) from the semicircle diameter are 25 Ω, 37 Ω, and 48 Ω for ZnSe@$Ti_3C_2T_x$, ZnSe and $Ti_3C_2T_x$, respectively. The minimum R_{ct} of ZnSe@$Ti_3C_2T_x$ indicates the lowest resistance for charge transfer during the redox reactions, demonstrating superior charge transfer at the electrode interface. The slope in the low-frequency

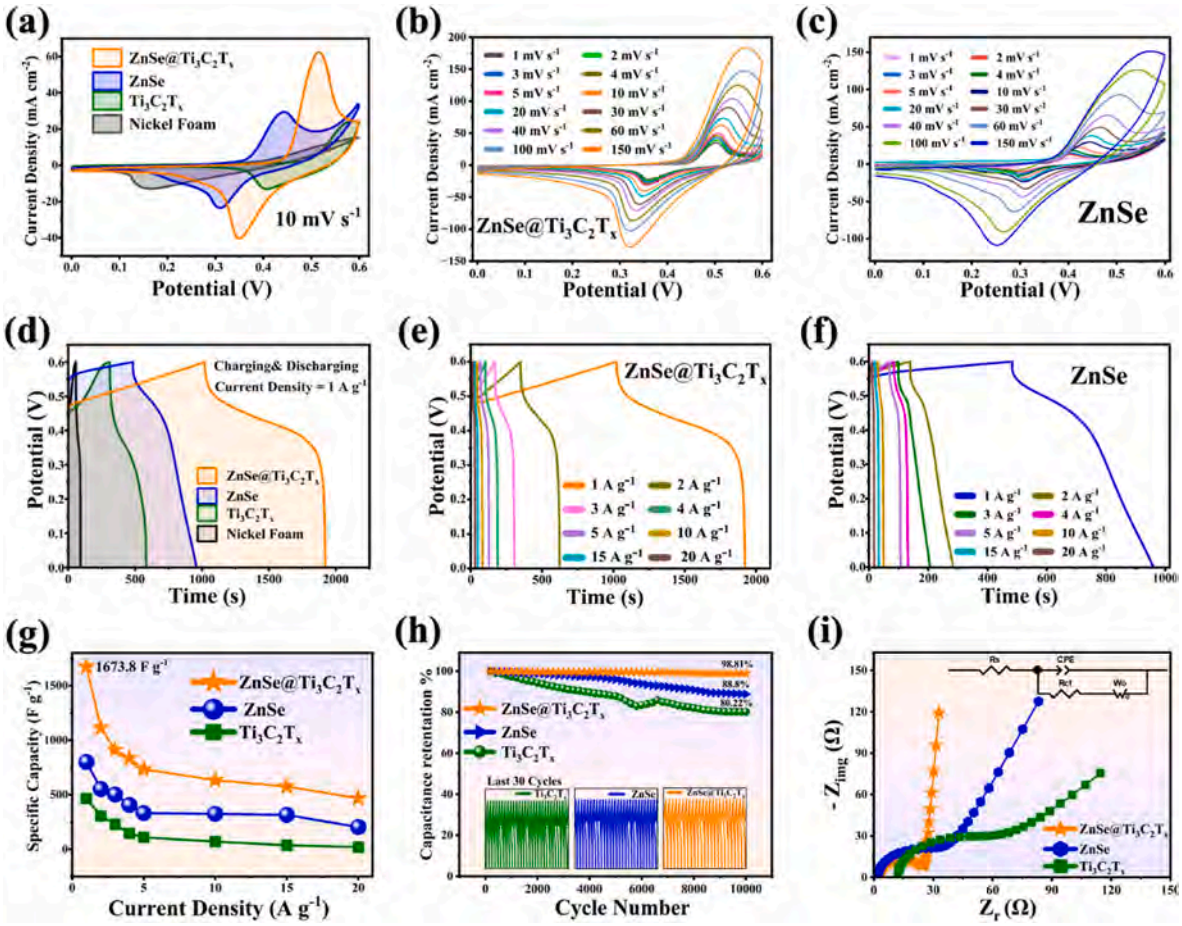

Fig. 4. (a) CV comparison at 10 mV s^{-1} scanning rate for ZnSe@$Ti_3C_2T_x$, ZnSe, $Ti_3C_2T_x$ and NF; CV curves at various scanning rates (1–150 mV s^{-1}) of (b) ZnSe@$Ti_3C_2T_x$ and (c) ZnSe; (d) GCD curves of NF and synthesized electrodes at 1 A g^{-1}; GCD curves at various current densities (1–20 A g^{-1}) of (e) ZnSe@$Ti_3C_2T_x$ and (f) ZnSe; (g) Capacity-current plots, (h) Capacity retention for 10,000 GCD cycles; (i) Nyquist plots.

region, determined by the Warburg constant (W_o), represents the ion conductivity. ZnSe@$Ti_3C_2T_x$ exhibits the steepest slope with minimum W_o demonstrating the highest ionic conductivity. The R_{ct} and W_o values are obtained by fitting the equivalent circuits of ZnSe@$Ti_3C_2T_x$ (Fig. 4i, Fig. S8a), ZnSe (Fig. S8b), and $Ti_3C_2T_x$ (Fig. S8c) also described in Table S1.

The CV curves disclose oxidation and reduction peaks, unequivocally indicating the occurrence of Faradaic redox reactions at the electrode-electrolyte interface. As shown in Fig. 5a and b, the anodic and cathodic properties (b values) of ZnSe and ZnSe@$Ti_3C_2T_x$ are examined to evaluate the contribution of capacitive and diffusion-controlled processes. The anodic and cathodic b values of ZnSe (0.51, 0.47) and ZnSe@$Ti_3C_2T_x$ (0.7, 0.8) reveal a diffusion-controlled effect for the ZnSe electrode, potentially attributed to the uncontrolled reaction of Zn. On the other hand, the ZnSe@$Ti_3C_2T_x$ electrode demonstrates a capacitive-controlled effect attributed to the synergistic effects of $Ti_3C_2T_x$, which not only prevents side reactions but also aids in the removal of agglomeration. Fig. 5c shows that incorporating $Ti_3C_2T_x$ into ZnSe enhances the pseudocapacitive properties with improved anodic and cathodic correlation coefficients (R^2) values (0.99, 0.96) compared to pristine ZnSe (0.983, 0.938). As shown in Fig. 5d, the CV of ZnSe reveals a pair of redox peaks at scanning rates ranging from 10, 20, 30, 40 and 60 mV s^{-1}. Dunn's method [56] is subsequently employed to delineate the pseudo-capacitance charge storage capabilities of both ZnSe and ZnSe@$Ti_3C_2T_x$ and categorize them into two distinct components. The first component pertains to surface capacitive contributions, known to enhance the power density, while the second component relates to diffusion-controlled contributions, which can similarly boost the transportation of charge carriers within the material. The inset illustrates the pseudocapacitive behavior of ZnSe, as evidenced by the redox peaks, highlighting that the majority of the capacitive contribution (71.7 %) stems from these peaks, with the remaining (28.3 %) attributed to diffusion processes at only 60 mV s^{-1}. Fig. 5e shows the pseudocapacitive behavior of the ZnSe electrode at different scanning rates (10–60 mV s^{-1}). The slopes (k_1) calculated and plotted at different potentials in Fig. 5f show the charging and discharging behavior for pseudo-capacitance as expressed by equation (1):

$$\frac{i(V)}{v^{1/2}} = k_1 v^{1/2} + k_2 \tag{1}$$

where *i(V)* shows the CV current at different voltages *(V)* in charging and discharging, *v* represents the scanning rate, and k_1 determined by software shows the slope of each curve, while the current is determined by $k_1 v$ at different voltages. To plot a graph for charging and discharging, $v^{1/2}$ (square root of scan rate) is set at abscissa, and $i(V)/v^{1/2}$ is selected as the ordinate. Fig. 5g and inset reveal a substantial enhancement in the current densities for ZnSe@$Ti_3C_2T_x$, indicating a more pronounced pseudocapacitive effect. At 60 mV s^{-1}, ZnSe@$Ti_3C_2T_x$ shows a pseudo-capacitance ratio of 88 % for the surface-controlled capacitive behavior. Fig. 5h shows the pseudocapacitive behavior of ZnSe@$Ti_3C_2T_x$ at different scanning rates (10–60 mV s^{-1}). The charging and discharging profiles of ZnSe@$Ti_3C_2T_x$ are presented in Fig. 5i using the same method for the ZnSe electrode. A comparative analysis of the pseudocapacitive contributions for both materials underscore the superior performance of ZnSe@$Ti_3C_2T_x$. Specifically, at a 10 mV s^{-1}, ZnSe shows only a 53 % capacitive contribution, whereas ZnSe@$Ti_3C_2T_x$

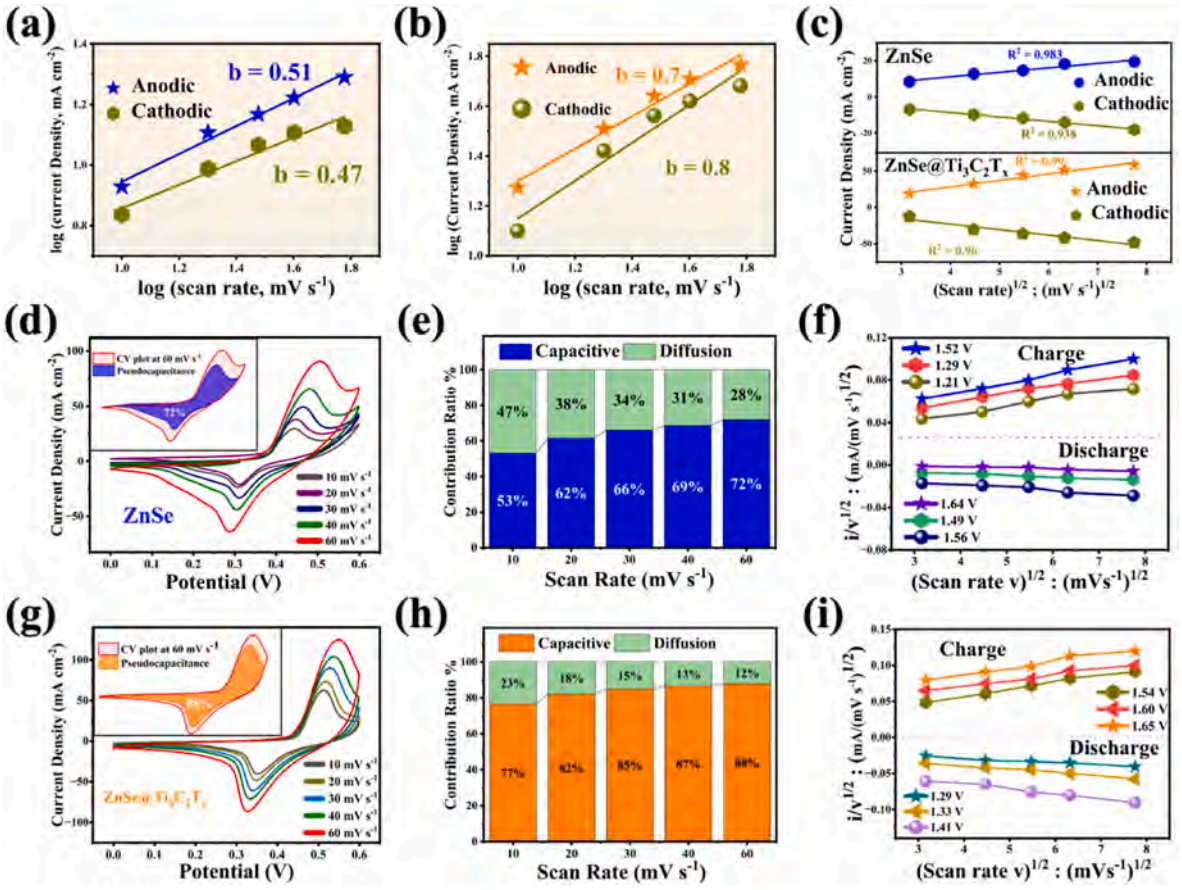

Fig. 5. b-values of (a) ZnSe and (b) ZnSe@$Ti_3C_2T_x$; (c) R^2 values from the anodic and cathodic peak currents; (d) CVs of the ZnSe electrode at scanning rates from 10 to 60 mV s^{-1} with the inset showing the % pseudo-capacitances at 60 mV s^{-1}; (e) Pseudocapacitive and diffusion controlled behavior of the ZnSe electrode; (f) Charging and discharging curves at various potentials; (g) CV curves of ZnSe@$Ti_3C_2T_x$ at scanning rates from 10 to 60 mV s^{-1} with the inset showing the pseudocapacitive contribution at a 60 mV s^{-1} scan rate; (h) Pseudocapacitive and Diffusion controlled behavior of ZnSe@$Ti_3C_2T_x$ at 10–60 mV s^{-1}; (i) Charging and discharging behavior at various potentials.

shows 77 %. The remarkable increase in maximum capacitive contribution of ZnSe@$Ti_3C_2T_x$ is primarily attributed to the incorporation of $Ti_3C_2T_x$, which exhibits excellent electrical conductivity and a significant surface area.

2.2. DFT calculations and practical assessment

DFT calculations are conducted to investigate the density of states, crystal structure, adsorption energy, and Fermi levels to study ion and electron transfer. Four computational models of Ti_3AlC_2, $Ti_3C_2T_x$, ZnSe, and ZnSe@$Ti_3C_2T_x$ are adopted. Fig. 6a and b shows the crystal structure of Ti_3AlC_2 where Al layers can be clearly observed. The obtained adsorption energies are determined to be negative as shown in Fig. 6c, which signifies more favorable thermodynamics and better adsorption potentials for the composite materials [57], as expressed by Eq. (2):

$$E_{ad} = E_{ZnSe@Ti_3C_2T_x:K} - E_{ZnSe} - E_{Ti_3C_2T_x:K} \quad (2)$$

ZnSe@$Ti_3C_2T_x$ has a higher adsorption energy of −3.228 eV than ZnSe (−1.432 eV) and $Ti_3C_2T_x$ (−2.112 eV). The higher adsorption energy can be attributed to the synergistic effects between ZnSe and $Ti_3C_2T_x$, indicating high stability. Fig. 6d–f shows the crystal structure, CTAB modification, and density of state (DOS) of ZnSe, where the dashed line displays the Fermi energy, while Zn and Se have the 2*p* and 3*d* orbitals, respectively. Fig. 6g–i demonstrates the crystal structure, band energy, and DOS of pure $Ti_3C_2T_x$, and Fig. 6j–l presents the crystal structure of ZnSe@$Ti_3C_2T_x$-interface and density of states DOS. The high intensity of DOS and extensive dispersion of ZnSe@$Ti_3C_2T_x$ -interface arise from the synergistic effects of $Ti_3C_2T_x$. The electronic states near the Fermi level are primarily contributed by Zn 2*p*, Se 3*d*, Ti 2*p*, and C 1*s* orbitals. In the ZnSe@$Ti_3C_2T_x$ electrode, Zn makes the main contribution, while the Se 3*d*, Ti 2*p*, and C 1*s* orbitals cross the Fermi level, suggesting that ZnSe@$Ti_3C_2T_x$ possesses a higher electron transfer rate than ZnSe and $Ti_3C_2T_x$. The exceptional electrical conductivity of $Ti_3C_2T_x$ and the presence of metallic Zn in the composite result in a high concentration of electrons near the Fermi level, contributing to accelerated electron transfer and improved reaction kinetics.

To assess the practical application of the ZnSe@$Ti_3C_2T_x$ electrode, the AC//ZnSe@$Ti_3C_2T_x$-APSC device is assembled, as shown in Fig. 7a, in which ZnSe@$Ti_3C_2T_x$ is the anode, AC is the cathode, and 7 M KOH is the electrolyte. In order to optimize the performance of the ZnSe@-$Ti_3C_2T_x$ electrode, the charge balance theorem is used to determine the appropriate mass of AC loaded on the cathode [58]. CV and GCD performance of AC is shown in Figs. S9a and b. The CV profiles of the ZnSe@$Ti_3C_2T_x$ electrode (0–0.6 V) and the AC electrode (−1 to 0 V) exhibit a remarkable concordance at a scanning rate of 10 mV s^{-1}, as shown in Fig. 7b. To investigate the maximum operating voltage range, CV experiments are conducted on the AC//ZnSe@$Ti_3C_2T_x$-APSC in the potential window from 0 to 1.7 V (Fig. 7c). The CV curves show a similar shape until the potential reaches 1.6 V, beyond which notable polarization occurs at the maximum voltage of 1.7 V due to precipitation of oxygen from the decomposition of water-based electrolytes, as indicated by the blue dotted circles [59]. However, the CV curve of the AC//ZnSe@$Ti_3C_2T_x$-APSC device maintains the integrity in the potential window of 0–1.6 V, indicating exceptional electrochemical stability

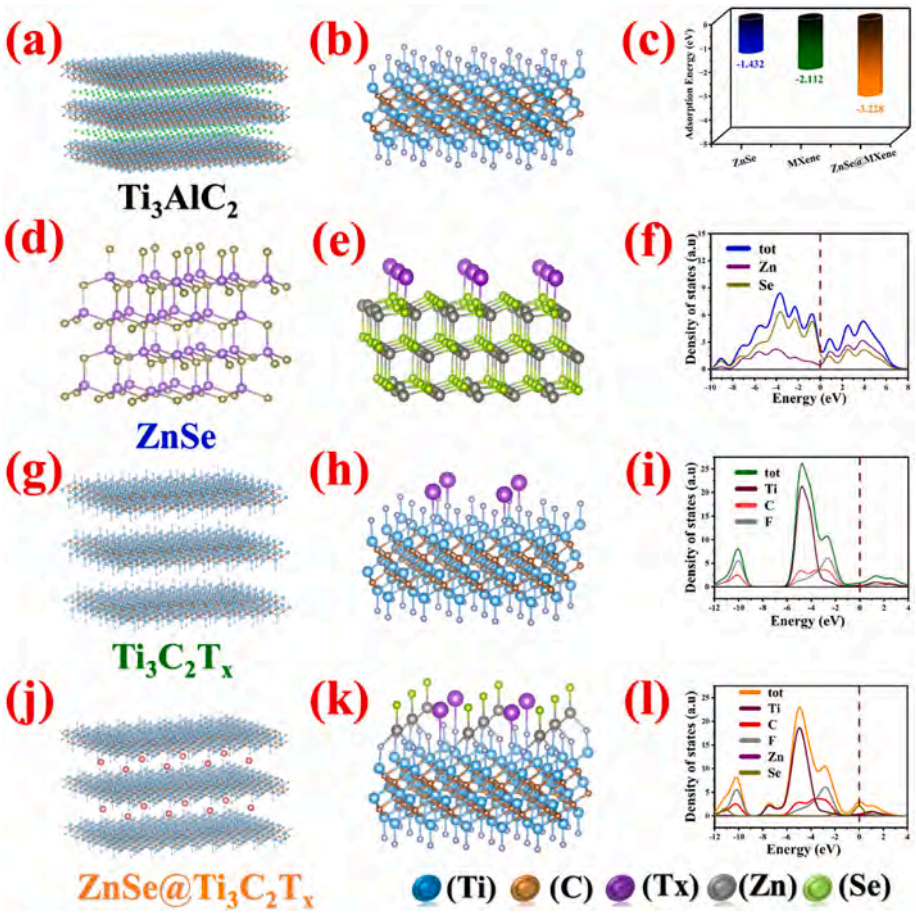

Fig. 6. (a–b) Ti_3AlC_2; (c) Adsorption energies of the samples; Structure, DFT simulations, and DOS graphs; (d–f) ZnSe, (g–i) $Ti_3C_2T_x$, and (j–l) ZnSe@$Ti_3C_2T_x$.

(Fig. 7d). Moreover, the area under the CV curve increases gradually, indicating outstanding electrochemical performance of the AC//ZnSe@$Ti_3C_2T_x$-APSC device.

GCD measurements are carried out (Fig. 7e) in current densities between 1 and 10 A g^{-1}. The exceptional regularity of the GCD curve of the AC//ZnSe@$Ti_3C_2T_x$-APSC device demonstrates an exceedingly reversible charging/discharging curve. The specific capacitances of the ZnSe@$Ti_3C_2T_x$-APSC calculated from the discharging time of the individual curves and the entire mass of the electrode materials deposited on the substrate are shown in Fig. 7f. The ZnSe@$Ti_3C_2T_x$-APSC exhibits a maximum specific capacitance of 259.12 F g^{-1} at 1 A g^{-1}, while the AC//ZnSe@$Ti_3C_2T_x$-APSC shows a specific capacitance of 149.54 F g^{-1} at 10 F g^{-1} and capacity of 57.7 %. As shown in Fig. 7g, the AC//ZnSe@$Ti_3C_2T_x$-APSC device attains the highest energy density of 92.90 Wh kg^{-1} at a power density (803.3 W kg^{-1}) and sustained a specific energy density of 54.60 Wh kg^{-1} (8.1 kW kg^{-1}). The final energy densities are compared to those of similar $Ti_3C_2T_x$/MXene-based materials. Our device demonstrates superiority compared to N-$Ti_3C_2T_x$-MXene//Zn (16.67 Wh kg^{-1} at a power density of 6004.8 W kg^{-1}) [60], NiCo$_2$Se/MXene//AC (23.7 Wh kg^{-1} at a power density of 800 W kg^{-1}) [61], CuS@MXene//Fe_2O_3@rGO (68.7 Wh kg^{-1} at a power density of 850 W kg^{-1}) [62], ($Ti_3C_2T_x$@Polyaniline//AC 12.8 Wh kg^{-1} at a power density of 985.8 W kg^{-1}) [63], ($MnCo_2S_4$MXene//AC 25.6 Wh kg^{-1} at a power density of 6400 W kg^{-1}) [64] and (NiCoMOF/MXene//AC 39.5 Wh kg^{-1} at a power density of 562.5 W kg^{-1}) [65].

Fig. 7h shows the Nyquist plots for the AC//ZnSe@$Ti_3C_2T_x$-APSC device at the initial cycle and after 10,000 cycles. APSC exhibits the lowest charge transfer resistance (R_{ct}) of 8 Ω after the stability test by EIS. The series resistance (R_s), Warburg impedance (R_w), and charge transfer resistance (R_{ct}) increase slightly after 10,000 cycles, as shown in Table S2. This increase in R_w after cycling stems from the complete penetration of the electrolyte. $Ti_3C_2T_x$ introduces surface defects in ZnSe to facilitate electron transfer by enhancing the conduction of electrons in the valence band. Frequency response of device is mentioned in Fig. S10.

The AC//ZnSe@$Ti_3C_2T_x$-APSC shows (Fig. 7i) outstanding pseudocapacitive properties of 80 % at a scanning rate of 50 mV s^{-1} in the potential window of 0–1.6 V. Similarly, the pseudocapacitive and diffusion phenomena are observed at 10, 20, 30, 40, and 50 mV s^{-1} showing the growing trend of the pseudo-capacitances of 64,71,75,78, and 80 %, respectively as shown in Fig. 7j. The b values are calculated at the same rates and different potentials of 1–1.6 V to determine the surface-controlled pseudocapacitive and diffusive properties shown in Fig. 7k. The AC//ZnSe@$Ti_3C_2T_x$-APSC device exhibits a remarkable capacitance retention rate 91.92 % after 10,000 cycles (Fig. 7l) indicating excellent electrochemical performance and a wide range of application prospects. The inset of Fig. 7l and Fig. S11 show the practical application of APSC.

The different performance underscores the potential of structural and electrochemical enhancements for advancing pseudocapacitive supercapacitors (PCSs) technology and positions ZnSe@$Ti_3C_2T_x$ as a compelling candidate for pseudo capacitors. The superior cycling stability and energy density of AC//ZnSe@$Ti_3C_2T_x$-APSC can be ascribed to three factors. Firstly, the $Ti_3C_2T_x$ nanosheets provide a large surface area, which acts as a physical barrier and offers more active sites for the deposition of active materials. Secondly, the incorporation of $Ti_3C_2T_x$ mitigates the agglomeration of ZnSe NPs and prevents side reactions of Zn. This enables ZnSe to provide more sites and a stable supply of Zn^{2+}, leading to enhanced reversibility and improved cyclic stability. The synergistic effects between ZnSe and $Ti_3C_2T_x$ significantly enhance the electrochemical performance of the APSC. Thirdly, the modification

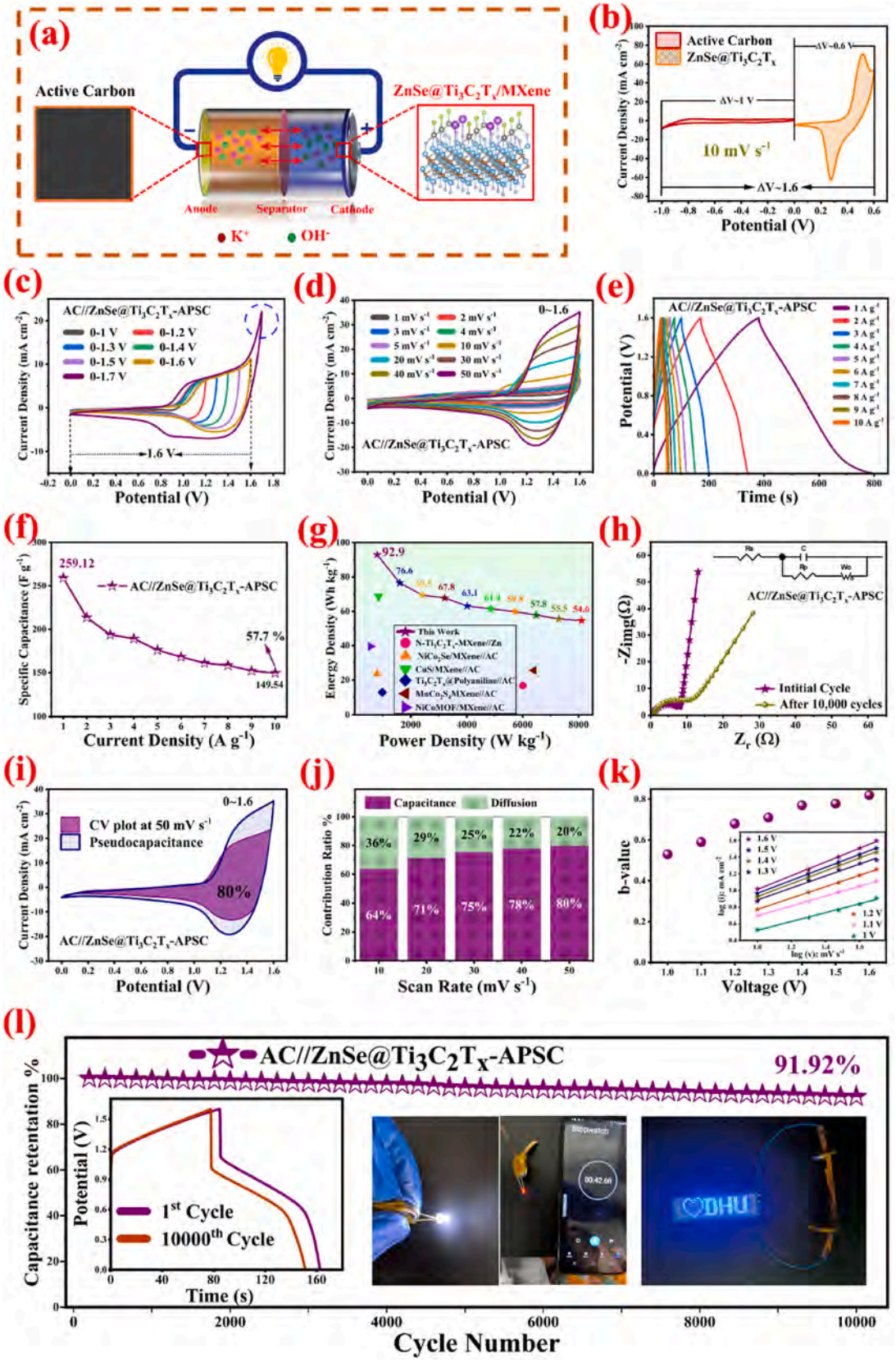

Fig. 7. Electrochemical properties of the AC//ZnSe@$Ti_3C_2T_x$-APSC device: (a) Schematic illustration of constructed APSC; (b) CV curve of the composite electrode versus AC at 10 mV s^{-1}; (c) CV curve of the APSC in different potential windows; (d) CV curves of the APSC at different current densities; (e) GCD curves at several scan rates in the potential window of 1–1.6 V; (f) Specific capacitance calculated at various current densities; (g) Ragone plot of AC//ZnSe@$Ti_3C_2T_x$-APSC and comparison with related published works; (h) Nyquist plots of the APSC; (i) Pseudo-capacitances of AC//ZnSe@$Ti_3C_2T_x$-APSC at 50 mV s^{-1}; (j) Capacitive and diffusion behavior at various scanning rates; (k) b values determined at different potentials; (l) Cyclic stability of the APSC for 10,000 cycles showing the initial and 10,000th cycle with the inset showing the practical application of the APSC device.

increases the surface activation energy, improves the efficiency of electrochemical reactions, and enhances the cycling stability.

2.3. Linear sweep voltammetry (LSV)

To evaluate the water-splitting capabilities with regard to OER and HER, comprehensive electrochemical assessments, including LSV, Tafel curves, and chronoamperometry, are undertaken at various scan rates. These methods shed light on the redox kinetics of NF, as well as synthesized $Ti_3C_2T_x$, ZnSe, and ZnSe@$Ti_3C_2T_x$ composite electrodes, using a 1 M KOH solution as the electrolyte. Specifically, LSV aims to ascertain the OER overpotential in the potential window of 1–2.6 (vs RHE) and HER (with a potential window 0.2 to -1V vs RHE) (Supporting section S6, Fig's. S12 and S13). The experimental findings of OER in Fig. 8a reveal a substantial decrease in overpotentials for ZnSe and ZnSe@-$Ti_3C_2T_x$ samples, with values of 234.3 mV and 185.4 mV, respectively.

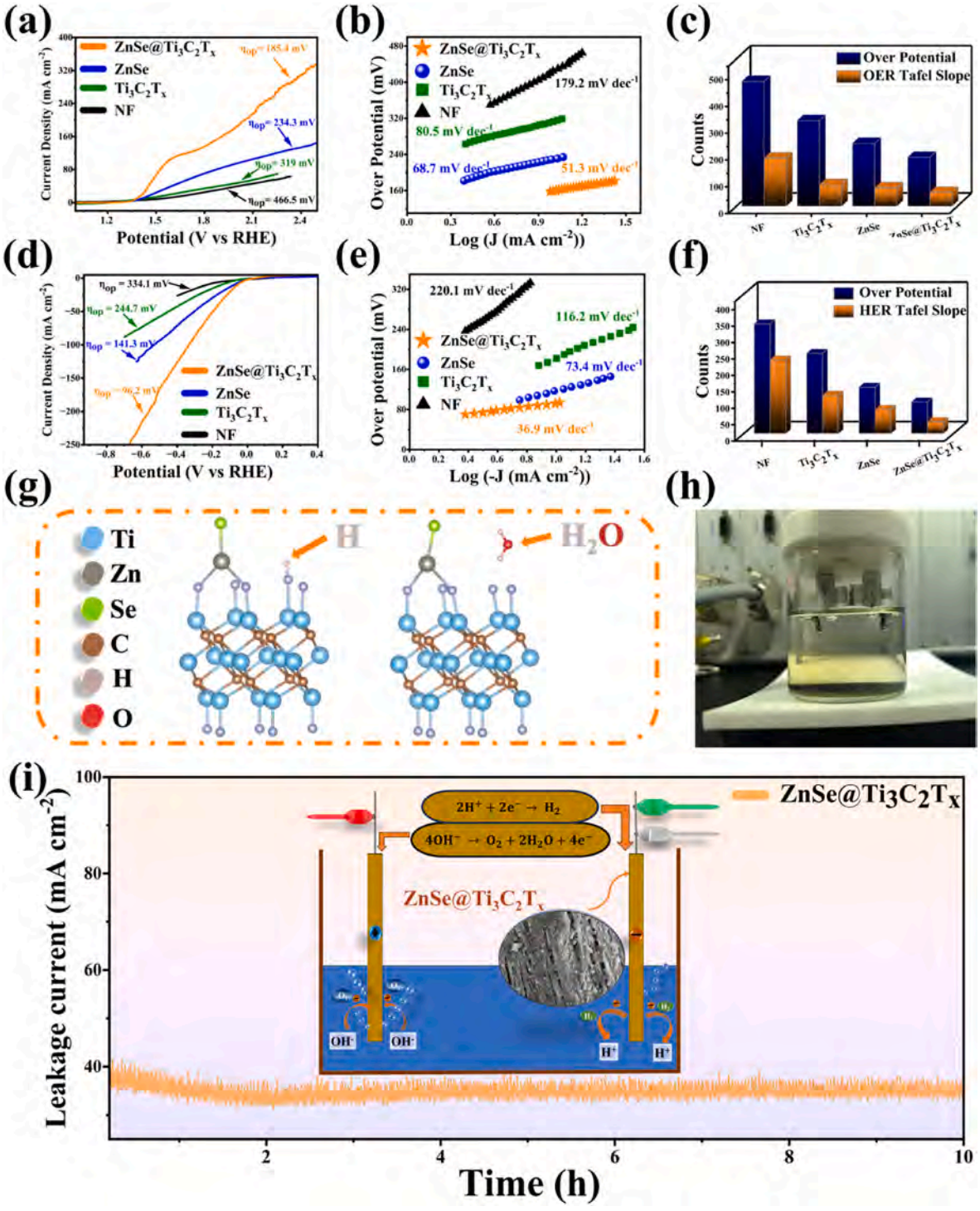

Fig. 8. OER and HER evaluation of NF (substrate), ZnSe, $Ti_3C_2T_x$, and ZnSe@$Ti_3C_2T_x$: (a) OER at a scanning rate of 5 mV s^{-1}; (b) Tafel plot for OER; (c) Tafel slopes and OER overpotentials; (d) HER at a scanning rate of 5 mV s^{-1}; (e) Tafel plot for HER; (f) Tafel slopes and HER overpotentials; (g) Atomic structure to calculate Gibbs free energy of H adsorption and H_2O adsorption; (h) experimental setup; (i) Long-term stability in water splitting at a current density of 40 mA cm^{-2}, with the inset showing the schematic illustration of HER/OER.

This reduction is in stark contrast to the higher values observed from NF and $Ti_3C_2T_x$ of 466.5 mV and 319 mV, respectively. The improvement in the catalytic performance can be attributed to the improved structural characteristics of ZnSe@$Ti_3C_2T_x$. Furthermore, Fig. 8b shows that ZnSe@$Ti_3C_2T_x$ is an exceptional catalyst with a Tafel slope of ~51.3 mV dec^{-1}. This finding contrasts with the weaker OER catalytic performance of NF and $Ti_3C_2T_x$, and the moderately better performance of ZnSe. The smaller Tafel slope of ZnSe@$Ti_3C_2T_x$ underscores its superior catalytic activity, making it highly favorable for OER applications. Fig. 8c compares the OER overpotentials and Tafel slopes of different electrocatalysts. As shown in Fig. 8d, the overpotentials of NF, $Ti_3C_2T_x$, ZnSe, and ZnSe@$Ti_3C_2T_x$ are in the 0.2 to −1 V potential range (vs RHE). NF and $Ti_3C_2T_x$ show higher overpotentials of 334.1 mV and 244.7 mV, respectively. In contrast, the ZnSe NPs show a marked reduction in the overpotential (141.3 mV), signifying better HER activity. This improvement is further amplified in the ZnSe@$Ti_3C_2T_x$ composite, with 96.2 mV overpotential. Fig. 8e shows the Tafel plots for HER, revealing suboptimal catalytic performance for NF and $Ti_3C_2T_x$, whereas ZnSe exhibits more favorable electrocatalytic behavior with a Tafel slope of 73.4 mV dec^{-1}. The most notable advance is observed from ZnSe@-$Ti_3C_2T_x$ which has the smallest Tafel slope of ~36.9 mV dec^{-1}. Fig. 8f compares the HER overpotentials and Tafel slopes. The Gibbs free energy calculations for hydrogen (H) and water (H_2O) adsorption on ZnSe@$Ti_3C_2T_x$ were performed using the VASP package, as shown in Fig. 8g, calculated by equation (3) and (4),

$$\Delta G_{ad} = E_{ZnSe@Ti_3C_2T_x:H} - E_{ZnSe@Ti_3C_2T_x} - E_H \ (for\ H) \quad (3)$$

$$\Delta G_{ad} = E_{ZnSe@Ti_3C_2T_x:H_2O} - E_{ZnSe@Ti_3C_2T_x} - E_{H_2O} \ (for\ H_2O) \quad (4)$$

The Gibbs free energy for hydrogen adsorption (ΔG_H) was found to be −2.22 eV, indicating strong interaction and efficient hydrogen atom binding, which enhances the HER kinetics. The Gibbs free energy for water adsorption (ΔG_{H_2O}) was −0.23 eV, reflecting a moderate interaction that facilitates water dissociation during the OER.

These results demonstrate the composite's dual capability in promoting both HER and OER, contributing to its excellent performance in water splitting, as further confirmed by the low Tafel slopes of ~51.3 mV dec^{-1} for OER and ~36.9 mV dec^{-1} for HER.

Fig. 8h shows the actual setup of overall water splitting. The Chronoamperometry test (Fig. S14) was performed to assess the stability of ZnSe, $Ti_3C_2T_x$, and ZnSe@$Ti_3C_2T_x$ under a constant current. As shown in (Fig. 8i) the ZnSe@$Ti_3C_2T_x$ composite maintains a high current density of 40 mA cm^{-1} for 10 h, demonstrating excellent stability as compare to ZnSe and $Ti_3C_2T_x$. This improved performance can be attributed to the enhanced conductivity of $Ti_3C_2T_x$, which facilitates efficient charge transport and supports the sustained current density in the composite, thereby improving its overall electrochemical stability [66]. The inset in Fig. 8i depicts a schematic representation of the electrolytic water splitting process, showing the generation of oxygen (O_2) at the anode and hydrogen (H_2) at the cathode.

3. Conclusion

In this study, the morphological and crystallographic properties of hydrothermally synthesized ZnSe microspheres are optimized. The synergistic effects rendered by the 2D-MXene nanosheets enhance the electrochemical performance in the APSC device as well as the water-splitting setup. The ZnSe electrode shows good electrochemical performance, but self-aggregation and side reactions of Zn restrict the performance of the cathode and applications. The $Ti_3C_2T_x$ nanosheets function as a physical barrier to alleviate agglomeration and impeding side reactions of Zn, thereby enabling ZnSe to expose more sites in addition to a consistent supply of Zn^{2+}, ultimately augmenting the reversibility, enhancing the cyclic stability, and diminishing the overpotential. The composite electrode demonstrates superior integrity and dispersion, resulting in a longer discharging time than the ZnSe electrode. The ZnSe@$Ti_3C_2T_x$ electrode shows outstanding cyclic stability (98.81 % capacity retention for 10,000 cycles), high specific capacitance of 1673.8 F g^{-1} at 1 A g^{-1}, and remarkable pseudocapacitive behavior of 88 % at 60 mV s^{-1}. DFT results confirm the higher adsorption energy, high electron density, and stable structure of the composite electrodes. The AC//ZnSe@$Ti_3C_2T_x$-APSC device demonstrates remarkable cyclic stability, energy density, and high specific capacitance boding well for energy storage applications. LSV reveals that the ZnSe@$Ti_3C_2T_x$ electrode has a remarkable tafel slope in OER (~51.3 mV dec^{-1}) compared to ZnSe (68.7 mV dec^{-1}) besides outstanding properties of ZnSe@$Ti_3C_2T_x$ in HER. This innovative approach effectively mitigates the inherent limitations of ZnSe and significantly enhances the overall electrochemical performance, positioning the ZnSe@$Ti_3C_2T_x$ as a promising candidate for energy storage and water splitting applications.

CRediT authorship contribution statement

Inaam Ullah: Writing – original draft, Validation, Software, Methodology, Investigation, Formal analysis, Data curation, Conceptualization. **Ayesha Irfan:** Investigation, Formal analysis, Conceptualization. **Mai Li:** Writing – review & editing, Visualization, Validation, Resources, Funding acquisition, Formal analysis. **Samira Saddique:** Investigation, Data curation. **Tiantian Yang:** Investigation. **Hanxue Zhao:** Investigation. **Nimra Irshad:** Investigation. **Kaishuai Yang:** Software. **Chunrui Wang:** Supervision. **Paul K. Chu:** Investigation, Funding acquisition.

Declaration of competing interest

The authors declare that there is no conflict of interest involved in any part of this article.

Acknowledgments

The research was funded by the Fundamental Research Funds for the Central Universities (No. 2232024D-31), National Natural Science Foundation of China (No. 22005046) and City University of Hong Kong Donation Research Grants (DON-RMG 9229021 and 9220061).

Appendix A. Supplementary data

Supplementary data to this article can be found online at https://doi.org/10.1016/j.jpowsour.2025.237046.

Data availability

Data will be made available on request.

References

[1] J. Balamurugan, Thanh Tuan Nguyen, Vanchiappan Aravindan, Nam Hoon Kim, Seung Hee Lee, Joong Hee Lee, All ternary metal selenide nanostructures for high energy flexible charge storage devices, Nano Energy 65 (2019) 103999, https://doi.org/10.1016/j.nanoen.2019.103999.

[2] R. Wang, W. Zhang, C. Reddy, R. Kakarla, C. Li, V. Gupta, J. Shim, T. Aminabhavi, Emerging two-dimensional (2D) MXene-based nanostructured materials: Synthesis strategies, properties, and applications as efficient pseudo-supercapacitors, Chemical Engineering Journal 472 (2023) https://doi.org/10.1016/j.cej.2023.144913..

[3] S. Ali, M. Javed, K. Umer, J. Wang, Y. Fu, S. Kong, S. Khan, A. Ahmad, A. Parkash, M. Albaqami, Annu, J. Qi, D. He, MoS2@ Ti3C2Tx Heterostructure: A new negative electrode material for Li-Ion hybrid supercapacitors, Chemical Engineering Journal 498 (2024) 155330. https://doi.org/10.1016/j.cej.2024.155330..

[4] H. Zhao, Wendong Xu, Mai Li, Zheyi Meng, Inaam Ullah, Muhammad Zubair Nawaz, Jiale Wang, Chunrui Wang, Paul K. Chu, Fe, co) oxide nanowires on gold nanoparticles modified MOF-Derived carbon nanoflakes for high-efficiency sodium-ion batteries and supercapacitors across electrolytes, J. Power Sources 626 (2025), https://doi.org/10.1016/j.jpowsour.2024.235793.

[5] Z.H.X. Li, C.E. Shuck, G. Liang, Y. Gogotsi, C. Zhi, MXene chemistry, electrochemistry and energy storage applications, Nat. Rev. Chem 6 (2022) 389–404, https://doi.org/10.1038/s41570-022-00384-8.

[6] S. Ali, Xiaofeng Zhang, Muhammad Sufyan Javed, Xiaqing Zhang, Guo Liu, Xuegang Wei, Hao Chen, Muhammad Imran, Jiatai Wang, Weihua Han, Jing Qi, 2H-MoS2 nanosheets-based binder-free electrode material for supercapacitor, J. Appl. Phys. 132 (2022), https://doi.org/10.1063/5.0100522.

[7] H. Wang, H. Niu, H. Wang, W. Wang, X. Jin, H. Wang, H. Zhou, T. Lin, Micro-meso porous structured carbon nanofibers with ultra-high surface area and large supercapacitor electrode capacitance, J. Power Sources 482 (2021) 228986, https://doi.org/10.1016/j.jpowsour.2020.228986.

[8] Y. Qiao, Yaling Wang, Xu Wang, Xin Dai, Guangjun Lv, Guopan Ren, Shengwu Guo, Wei Wang, Lei Li, Yuanzhen Chen, Preparation of hierarchical porous carbon sieve through the decomposition-templating of NaHCO3 for high areal energy density micro-supercapacitor, Chem. Eng. J. 488 (2024) 150843, https://doi.org/10.1016/j.cej.2024.150843.

[9] H.X.G. Zhang, J. Yang, R. Wang, Z. Xie, X. Liang, P. Han, Y. Wu, Preparation and characterization of novel 2D/3D NiSe2/MnSe grown on rGO/Ni foam for high performance battery-supercapacitor hybrid devices, J. Power Sources 506 (2021) 230255, https://doi.org/10.1016/j.jpowsour.2021.230255.

[10] A. Davarani, Construction of complex copper-cobalt selenide hollow structures as an attractive battery-type electrode material for hybrid supercapacitors, Chem. Eng. J 402 (2020) 126241. https://doi.org/10.1016/j.cej.2020.126241.

[11] H.S.X.H. Zheng, J. Hu, H. Liu, L. Wei, S. Wu, Y. Huang, J. Li, K. Tang, Construction of hierarchical MnSe@SnSe2@N-C nanorods for high-performance lithium-ion batteries, ACS Appl. Energy Mater. 5 (2022) 6586–6596, https://doi.org/10.1021/acsaem.2c01293.

[12] Q.Y.Y. Chen, P. Wu, T. Xu, J. Wang, Y. Li, Metal-complex-assisted synthesis of SnSe nanorods for lithium-ion-battery anodes, ACS Appl. Nano Mater. 4 (2021) 13010–13017, https://doi.org/10.1021/acsanm.1c02356.

[13] S. Wang, Tianyu Li, Yanbin Yin, Nana Chang, Huamin Zhang, Xianfeng Li, High-energy-density aqueous zinc-based hybrid supercapacitor-battery with uniform zinc deposition achieved by multifunctional decoupled additive, Nano Energy 96 (2022) 107120, https://doi.org/10.1016/j.nanoen.2022.107120.

[14] S. Ali, X. Zhang, M S. Javed, H U. Shah, A. Ahmad, M. D. Albaqami, M. Sheikh, A M. Hassan, X. Wei, J. Wang, J. Qi, MoS2/Ti3CO2 heterostructure-based ceramics as promising electrode material for high-performance monovalent energy storage devices, Ceramics International, 50 (2024) 4782-4789. https://doi.org/10.1016/j.ceramint.2023.11.222..

[15] H. Wang, Meng Wang, Yongbing Tang, A novel zinc-ion hybrid supercapacitor for long-life and low-cost energy storage applications, Energy Storage Mater. 13 (2018) 1–7, https://doi.org/10.1016/j.ensm.2017.12.022.

[16] I. Ullah, Jolly Jacob, F.F. Al-Harbi, K. Mahmood, A. Ali, M. Tamseel, Salma Ikram, N. Amin, K. Javaid, Lamia Ben Farhat, S. Hussain, M. Yasir Ali, Investigating the potential of AgZnO thin film composites for waste heat recovery using seebeck data, Opt. Mater. 127 (2022), https://doi.org/10.1016/j.optmat.2022.112318.

[17] X. Xu, Bo Mai, Zhengbo Liu, Shaomin Ji, Renzong Hu, Liuzhang Ouyang, Jun Liu, Min Zhu, Self-sacrificial template-directed ZnSe@ C as high performance anode for potassium-ion batteries, Chem. Eng. J. 387 (2020), https://doi.org/10.1016/j.cej.2020.124061.

[18] B. Feng, Jian Cao, Donglai Han, Hongtao Liang, Shuo Yang, Xiuyan Li, Jinghai Yang, ZnSe nanoparticles of different sizes: optical and photocatalytic properties, Mater. Sci. Semicond. Process. 27 (2014) 865–872, https://doi.org/10.1016/j.mssp.2014.08.027.

[19] Y. Fu, Zhian Zhang, Ke Du, Yaohui Qu, Qiang Li, Xing Yang, Spherical-like ZnSe with facile synthesis as a potential electrode material for lithium-ion batteries, Mater. Lett. 146 (2015) 96–98, https://doi.org/10.1016/j.matlet.2015.02.019.

[20] S. Ali, Muhammad Ahsan Farooq Qaisar, Muhammad Sufyan Javed, Khalid Umer, Saleh S. Alarfaji, Muhammad Mateen, Muhammad Chhattal, Shafqat Ali, Anand Parkash, Tensangmu Lama Tamang, Jing Qi, Two-dimensional MXene based innovative electrode materials for supercapacitors: recent advances and prospects, Fuel 377 (2024) 132783, https://doi.org/10.1016/j.fuel.2024.132783.

[21] C. Zhang, L. McKeon, M.P. Kremer, S.-H. Park, O. Ronan, A. Seral-Ascaso, S. Barwich, C.Ó. Coileáin, N. McEvoy, H.C. Nerl, B. Anasori, J.N. Coleman, Y. Gogotsi, V. Nicolosi, Additive-free MXene inks and direct printing of micro-supercapacitors, Nat. Commun. 10 (2019). https://www.nature.com/articles/s41467-019-09398-1.

[22] H.-T. Kwon, Cheol-Min Park, Electrochemical characteristics of ZnSe and its nanostructured composite for rechargeable Li-ion batteries, J. Power Sources 251 (2014) 319–324, https://doi.org/10.1016/j.jpowsour.2013.11.033.

[23] W.-D. Yang, Rong-Da Zhao, Fang-Yu Guo, Jun Xiang, Sroeurb Loy, Liang Liu, Jia-Yu Dai, Fu-Fa Wu, Interface engineering of hybrid ZnCo2O4@ Ni2. 5Mo6S6. 7 structures for flexible energy storage and alkaline water splitting, Chem. Eng. J. 454 (2023) 140458, https://doi.org/10.1016/j.cej.2022.140458.

[24] W.-D. Yang, Rong-Da Zhao, Jun Xiang, Sroeurb Loy, Yi-Fei Di, Li Jia, Mei-Ting Li, Dong-Mei Ma, Fu-Fa Wu, 3D hierarchical ZnCo2S4@ Ni (OH) 2 nanowire arrays with excellent flexible energy storage and electrocatalytic performance, J. Colloid Interface Sci. 626 (2022) 866–878, https://doi.org/10.1016/j.jcis.2022.07.020.

[25] A. Irfan, I. Ullah, M. Li, W. Xu, Z. Dong, H. Zhao, H. Hu, N. Irshad, K. Yang, P. Zhong, P.K. Chu, Synergistic effects of hybrid CuS@ Ti3C2Tx/MXene material for enhanced super capacitive energy storage and efficient water splitting, Surf. Interfaces 56 (2024) 105536, https://doi.org/10.1016/j.surfin.2024.105536.

[26] S. Ali, Tauqeer Ahmad, Muhammad Yahya Tahir, Muhammad Usman, Muhammad Chhattal, Iftikhar Hussain, Shaukat Khan, Ahmed M. Hassan, Mohammed A. Assiri, P. Rosaiah, Muhammad Sufyan Javed, Bhargav Akkinepally, Jing Qi, The emergence of density functional theory for supercapacitors: recent progress and advances, J. Energy Storage 73 (2023), https://doi.org/10.1016/j.est.2023.109100.

[27] Y. Xie, Haitao Zhang, Haichao Huang, Zixing Wang, Zhong Xu, Haibo Zhao, Yuchen Wang, Ningjun Chen, Weiqing Yang, High-voltage asymmetric MXene-based on-chip micro-supercapacitors, Nano Energy 74 (2020), https://doi.org/10.1016/j.nanoen.2020.104928.

[28] R.B.W.Z.L. Chen, H. Wang, K.H.L. Zhang, Y. Song, F.L. Wu, F. Fang, D.L. Sun, Embedding ZnSe nanodots in nitrogen-doped hollow carbon architectures for superior lithium storage, Nano Res. 11 (2017) 966–978. https://link.springer.com/article/10.1007/s12274-017-1709-x.

[29] X. Wendong, Mai Li, Waqar ul Hasan, Zheyi Meng, Haotian Hu, Inaam Ullah, Ayesha Irfan, Jiayi Shen, Paul K. Chu, Composition-optimized NiGa-LDH on MOF-Derived and cobalt-nanoparticles-embedded carbon flakes for enhanced potassium-ion storage, Chem. Eng. J. 499 (2024), https://doi.org/10.1016/j.cej.2024.155931.

[30] B.M.X.J. Xu, Z.B. Liu, S.M. Ji, R.Z. Hu, L.Z. Ouyang, J. Liu, M. Zhu, Self sacrificial template-directed ZnSe@C as high performance anode for potassium-ion batteries, Chem. Eng. J 387 (2020), https://doi.org/10.1016/j.cej.2020.124061.

[31] T. Zhang, Daping Qiu, and Yanglong Hou., Free-standing and consecutive ZnSe@ carbon nanofibers architectures as ultra-long lifespan anode for flexible lithium-ion batteries, Nano Energy 94 ..

[32] B. Shen, Xianjin Hu, Hai-Tao Ren, Hao-Kai Peng, Bing-Chiuan Shiu, Jia-Horng Lin, Ching-Wen Lou, Ting-Ting Li, Rosette-like (ni, co) Se2@ Nb2CTx MXene heterostructure with abundant Se vacancies for high-performance flexible supercapacitor electrodes, Chem. Eng. J. (2024), https://doi.org/10.1016/j.cej.2024.149440.

[33] X. Wang, Liubing Dong, Wenbao Liu, Yongfeng Huang, Xuechao Pu, Jinjie Wang, Feiyu Kang, Li Jia, Chengjun Xu, Few-layer Ti3C2Tx MXene delaminated via flash freezing for high-rate electrochemical capacitive energy storage, J. Energy Chem. 48 (2020) 233–240, https://doi.org/10.1016/j.jechem.2020.01.006.

[34] S.-L. Xu, Rong-Da. Zhao, Rui-Yu. Li, J. Li, J. Xiang, Fang-Yu. Guo, J. Qi, L. Liu, Fu-Fa. Wu, Constructing high-performance supercapacitors and electrochemical water splitting electrode materials through core–shell structured Co9S8@Ni(OH)2 nanosheets, Journal of Materials Chemistry (2024)..

[35] N. Chen, Yihao Zhou, Songlin Zhang, Haichao Huang, Chuanfang John Zhang, Xiaotong Zheng, Xiang Chu, Haitao Zhang, Weiqing Yang, Jun Chen, Tailoring Ti3CNTx MXene via an acid molecular scissor, Nano Energy 85 (2021), https://doi.org/10.1016/j.nanoen.2021.106007.

[36] P. Lian, Yanfeng Dong, Zhong-Shuai Wu, Shuanghao Zheng, Xiaohui Wang, Sen Wang, Chenglin Sun, Jieqiong Qin, Xiaoyu Shi, Xinhe Bao, Alkalized Ti3C2 MXene nanoribbons with expanded interlayer spacing for high-capacity sodium and potassium ion batteries, Nano Energy 40 (2017) 1–8, https://doi.org/10.1016/j.nanoen.2017.08.002.

[37] H. Huang, Jiaqi He, Zixing Wang, Haitao Zhang, Long Jin, Ningjun Chen, Yanting Xie, Xiang Chu, Bingni Gu, Weili Deng, Weiqing Yang, Scalable, and low-cost treating-cutting-coating manufacture platform for MXene-based on-chip micro-supercapacitors, Nano Energy 69 (2020) 104431, https://doi.org/10.1016/j.nanoen.2019.104431.

[38] Y. Pei, Xiaoli Zhang, Zengyu Hui, Jinyuan Zhou, Xiao Huang, Gengzhi Sun, Wei Huang, Ti3C2TX MXene for sensing applications: recent progress, design principles, and future perspectives, ACS Nano 15 (2021), https://doi.org/10.1021/acsnano.1c00248.

[39] R. Karkuzhali, Shanmugasundaram Manoj, Karnan Shanmugapriya, Alam Venugopal Narendra Kumar, Gopalakrishnan Gopu, N. Muniyappan, Byong-hun jeon, and subbaiah muthu prabhu, MXene-based O/Se-rich bimetallic nanocomposites for high performance solid-state symmetric supercapacitors, J. Solid State Chem. 306 (2022), https://doi.org/10.1016/j.jssc.2021.122727.

[40] Y. Li, Song-Lin Xu, Zi-Qing Ai, Jin-Gang Qi, Fu-Fa Wu, Rong-Da Zhao, Zhao De-Peng, Interface engineering accelerated surface reconstruction for electrocatalytic water splitting and energy storage device through hybrid structured ZnCo2O4@ NiCo-LDH nanocomposite, International Journal of Hydrogen Energy 91 (2024) 867–876, https://doi.org/10.1016/j.ijhydene.2024.10.104.

[41] K. Dashtian, Samaneh Shahsavarifar, Muhammad Usman, Yvonne Joseph, Mohammad Reza Ganjali, Zongyou Yin, Mehdi Rahimi-Nasrabadi, A comprehensive review on advances in polyoxometalate based materials for electrochemical water splitting, Coord. Chem. Rev. 504 (2024), https://doi.org/10.1016/j.ccr.2023.215644.

[42] Z. Dong, Zhaoyang Wang, Tiantian Yang, Hange Feng, Lingwei Li, Inaam Ullah, Shaolin Xue, Photocatalytic hydrogen production and simultaneous tetracycline degradation by selectively depositing growth of MoS2 on the PbTiO3 683, Colloids and Surfaces A Physicochemical and Engineering Aspects. (2024) 133096, https://doi.org/10.1016/j.colsurfa.2023.133096.

[43] D. Wang, Yu-Xin Chang, Ya-Ru Li, Shi-Lin Zhang, Sai-Long Xu, Well-dispersed NiCoS2 nanoparticles/rGO composite with a large specific surface area as an oxygen evolution reaction electrocatalyst, Rare Met. 40 (2021) 3156–3165. https://link.springer.com/article/10.1007/s12598-021-01733-0.

[44] Y. Chen, Lijuan Wang, Wenzhong Wang, Maosheng Cao, Enhanced photoelectrochemical properties of ZnO/ZnSe/CdSe/Cu2-xSe core–shell nanowire arrays fabricated by ion-replacement method, Appl. Catal. B Environ. 209 (2017) 110–117, https://doi.org/10.1016/j.apcatb.2017.02.049.

[45] Z. Wang, Shuling Liu, Wen Duan, Yichuang Xing, Yanling Hu, Yujie Ma, Transition metal selenides as catalysts for electrochemical water splitting, Int. J. Hydrogen Energy 60 (2024) 1414–1432, https://doi.org/10.1016/j.ijhydene.2024.02.201.

[46] M. Saquib, Nitish Srivastava, Pratham Arora, Amit C. Bhosale, NiMoSe/$Ti_3C_2T_x$ MXene@CC as a highly operative bifunctional electrocatalyst for hydrogen and oxygen evolution reactions in an alkaline medium, Int. J. Hydrogen Energy 59 (2024) 1132–1142, https://doi.org/10.1016/j.ijhydene.2024.02.100.

[47] E. Ceesay, M. Waqas Hakim, Eisha Mazhar, SaifUllah Awan, Syed Rizwan, Improved pseudocapacitor and water splitting in cobalt-anchored vanadium carbide MXene nanocomposite, Int. J. Hydrogen Energy 56 (2024), https://doi.org/10.1016/j.ijhydene.2023.12.066.

[48] J. Ma, Yujuan Cheng, Lei Wang, Xiaohu Dai, Fei Yu, Free-standing $Ti_3C_2T_x$ MXene film as binder-free electrode in capacitive deionization with an ultrahigh desalination capacity, Chem. Eng. J. 384 (2020), https://doi.org/10.1016/j.cej.2019.123329.

[49] Z. Wang, Sangxin Liu, Qirui Hou, Licui Zhang, Anping Zhang, Feng Li, Xiukui Zhang, Ping Wu, Xiaoshu Zhu, Wei Shaohua, Yiming Zhou, Confining ultrafine ZnSe nanoparticles in N, Se-codoped carbon matrix using a direct solid state reaction approach for boosting sodium storage performance, J. Alloys Compd. 840 (2020), https://doi.org/10.1016/j.jallcom.2020.155703.

[50] G. Lu, Huizi An, Yu Chen, Jiehui Huang, Hongzhou Zhang, Bin Xiang, Qing Zhao, Dapeng Yu, Weimin Du, Temperature dependence of raman scattering of ZnSe nanoparticle grown through vapor phase, J. Cryst. Growth 274 (2005) 530–535, https://doi.org/10.1016/j.jcrysgro.2004.10.062.

[51] R.Z.D. Zhao, S. Dong, X. Miao, Z. Zhang, C. Wang, L. Yin, Alkali-induced 3D crinkled porous Ti_3C_2 MXene architectures coupled with NiCoP bimetallic phosphide nanoparticles as anodes for high-performance sodium-ion batteries, Energy Environ. Sci. 12 (2019) 2422–2432, https://doi.org/10.1039/C9EE00308H.

[52] K. Feng, Wenhua Xue, Xiaoyun Hu, Jun Fan, Enzhou Liu, Z-scheme CdSe/ZnSe heterojunction for efficient photocatalytic hydrogen evolution, Colloids Surf. A Physicochem. Eng. Asp. 622 (2021), https://doi.org/10.1016/j.colsurfa.2021.126633.

[53] J.R. Shallenberger, Niklas Hellgren, Zinc selenide analyzed by XPS, Surf. Sci. Spectra 27 (2020). https://pubs.aip.org/avs/sss/article/27/1/014020/367017.

[54] S.A.S. De, S. Sahoo, J.J. Shim, G.C. Nayak, From 0D to 3D MXenes: their diverse syntheses, morphologies and applications, Mater. Chem. Front. 6 (2022), https://doi.org/10.1039/D2QM00002D.

[55] Y.Z.N. Li, M. Jia, X. Lv, X. Li, R. Li, X. Ding, Y.-Z. Zheng, X. Tao, 1T/2H $MoSe_2$-on-MXene heterostructure as bifunctional electrocatalyst for efficient overall water splitting, Electrochim. Acta 326 (2019), https://doi.org/10.1016/j.electacta.2019.134976.

[56] J. Liu, Jin Wang, Chaohe Xu, Hao Jiang, Chunzhong Li, Lili Zhang, Jianyi Lin, Ze Xiang Shen, Advanced energy storage devices: basic principles, analytical methods, and rational materials design, Adv. Sci. 5 (2018), https://doi.org/10.1002/advs.201700322.

[57] M.S. Javed, Muhammad Kashif Aslam, Sumreen Asim, Saima Batool, Muhammad Idrees, Shahid Hussain, Syed Shoaib Ahmad Shah, Muhammad Saleem, Wenjie Mai, Chenguo Hu, High-performance flexible hybrid-supercapacitor enabled by pairing binder-free ultrathin ni–co–o nanosheets and metal-organic framework derived N-doped carbon nanosheets, Electrochim. Acta 349 (2020), https://doi.org/10.1016/j.electacta.2020.136384.

[58] J. Zhang, Xiaodong Lu, Jingjing Zhang, Han Li, Bowen Huang, Bingbing Chen, Jianqiu Zhou, Suming Jing, Metal-ions intercalation mechanism in layered anode from first-principles calculation, Front. Chem. 9 (2021), https://doi.org/10.3389/fchem.2021.677620.

[59] J. Fu, Lei Li, Je Moon Yun, Damin Lee, Bong Ki Ryu, Kwang Ho Kim, Two-dimensional titanium carbide (MXene)-wrapped sisal-like $NiCo_2S_4$ as positive electrode for high-performance hybrid pouch-type asymmetric supercapacitor, Chem. Eng. J. 375 (2019), https://doi.org/10.1016/j.cej.2019.121939.

[60] A. Mateen, Mohd Zahid Ansari, Qasim Abbas, Muneeb Ahmed, Ahmad Hussain, Elsayed Tag Eldin, Fatimah Mohammed Alzahrani, Norah Salem Alsaiari, Shafaqat Ali, Muhammad Sufyan Javed, In situ nitrogen functionalization of 2D-$Ti_3C_2T_x$-MXenes for high-performance Zn-ion supercapacitor, Molecules 27 (2022), https://doi.org/10.3390/molecules27217446.

[61] J.G.Y. Liu, J. Wang, C. Hu, M. Xie, X. Jin, S. Wang, Y. Dai, Facile fabrication of MXene supported nickel-cobalt selenide ternary composite via one-step hydrothermal for high-performance asymmetric supercapacitors, J. Alloy. Compd 899 (2022), https://doi.org/10.1016/j.jallcom.2021.163354.

[62] X. Chen, Huiran Ge, Wen Yang, Jianli Liu, Peizhi Yang, Construction of high-performance solid-state asymmetric supercapacitor based on $Ti_3C_2T_x$ MXene/CuS positive electrode and Fe_2O_3@rGO negative electrode, J. Energy Storage 68 (2023), https://doi.org/10.1016/j.est.2023.107700.

[63] J.J. Fu, JeMoon Yun, Shuxing Wu, Lei Li, Litao Yu, Kwang Ho Kim, Architecturally robust graphene-encapsulated MXene Ti_2CT_x@ polyaniline composite for high-performance pouch-type asymmetric supercapacitor, ACS Appl. Mater. Interfaces 10 (2018) 34212–34221, https://doi.org/10.1021/acsami.8b10195.

[64] K. Nasrin, K. Subramani, M. Karnan, M. Sathish, $MnCo_2S_4$–MXene: a novel hybrid electrode material for high performance long-life asymmetric supercapattery, J. Colloid Interface Sci. 600 (2021) 264–277, https://doi.org/10.1016/j.jcis.2021.05.037.

[65] Y. Wang, Yuexin Liu, Chao Wang, Hu Liu, Jiaoxia Zhang, Jing Lin, Jincheng Fan, Tao Ding, Jong E. Ryu, Zhanhu Guo, Significantly enhanced ultrathin NiCo-based MOF nanosheet electrodes hybrided with Ti3C2Tx MXene for high performance asymmetric supercapacitor, Eng. Sci. 9 (2020) 50–59, https://doi.org/10.30919/es8d903.

[66] J. Li, Zeqiong. Zhao, Yuanyuan. Ma, Yongquan. Qu, Graphene and their hybrid electrocatalysts for water splitting, ChemCatChem 9 (2017) 1554-1568. https://doi.org/10.1002/cctc.201700175: .

Supporting Information

Optimizing ZnSe Microspheres through 2D MXene for Asymmetric Pseudocapacitive Supercapacitors and Efficient Hydrogen Production via Water Splitting

Inaam Ullah[a], Ayesha Irfan[a], Mai Li[a*], Samira Saddique[b], Yang Tiantian[a], Hanxue Zhao[a], Nimra Irshad[a], Kaishuai Yang[c*], Chunrui Wang[a*] Paul K. Chu[d]

[a] College of Science, Donghua University, Shanghai 201620, China

[b] School of Materials Science and Engineering, University of Science and Technology Beijing, Beijing 100083, China

[c] School of Electronic and Information Engineering, Changshu Institute of Technology, Suzhou 215000, P. R. China

[d] Department of Physics, Department of Materials Science and Engineering, and Department of Biomedical Engineering, City University of Hong Kong, Tat Chee Avenue, Kowloon, Hong Kong, China

* Corresponding authors: E-mail: limai@dhu.edu.cn (M. Li); crwang@dhu.edu.cn (Chunrui Wang); ksyang@cslg.edu.cn (Kaishuai Yang)

Contents:

S1. Materials and Method:

High-purity reagents were used to synthesize ZnSe nanoparticles, including zinc chloride ($ZnCl_2$) and selenium powder (99.99% purity), both sourced from Sinopharm Chemical Reagent Co., Ltd. Sodium sulfite (Na_2SO_3), deionized water, ethanol, and methanol were also employed in the synthesis. For the preparation of $Ti_3C_2T_x$, MAX phase powder, LiF, and HCl were obtained from Shanghai Macklin Biochemical Co., Ltd. All materials were of analytical grade and used without further purification.

S1.1. Synthesis of ZnSe nanoparticles:

The synthesis of ZnSe nanoparticles was carried out by dissolving 1 g of 99.99% pure zinc chloride ($ZnCl_2$) in 20 ml deionized water, 0.3 g of 99.99% pure selenium powder in 20 ml deionized water, and 2 g of 99.99% pure sodium sulfite (Na_2SO_3) in 50 ml deionized water. Each solution was stirred magnetically for 30 minutes, mixed together, and stirred again for another 30 minutes. The mixed solution was then transferred to a 100 ml autoclave and heated at 200°C for 22 hours. The resulting precipitate was centrifuged at 3500 rpm for 10 minutes to obtain a powder, which was then vacuum-filtered and washed multiple times with deionized water and ethanol to remove impurities. Finally, the powder was vacuum-dried at 0.1 pascal and 60°C for 6 hours. The synthesis mechanism is illustrated by the following chemical equations:

$$ZnCl_2 + Se + Na_2SO_3 + H_2O \rightarrow ZnSe + Na_2SO_4 + 2HCl ----Eq\ S1$$

After the hydrothermal synthesis of ZnSe spheres, CTAB was used as a surfactant to modify the surface properties of ZnSe. The CTAB treatment stabilized the ZnSe particles by preventing aggregation and improving their dispersion in solution. Additionally, CTAB's cationic surfactant properties enhanced the surface reactivity of ZnSe microspheres.

we have investigated the morphology and crystal growth of ZnSe microspheres at different reaction temperatures (**180°C, 200°C, and 220°C**) and varied reaction times. Our observations show that the most uniform microspheres with the smallest crystal size were obtained at **200°C** with a reaction time of **22 hours**. At this condition, the ZnSe microspheres were self-agglomerated, as seen in the SEM images provided below, which demonstrate well-defined and uniform structures.

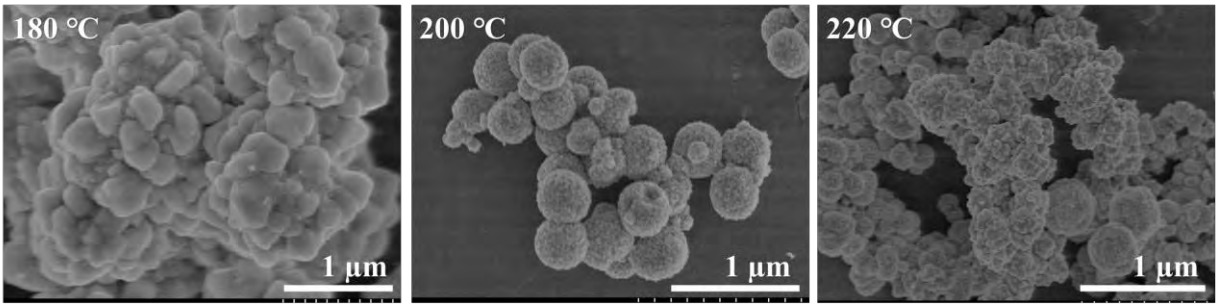

S1.2. Synthesis of $Ti_3C_2T_x$ by MAX powder:

The synthesis of $Ti_3C_2T_x$ from MAX powder entailed a multi-step process. Initially, 2 g of LiF was dissolved in 40 ml of HCl and stirred for 30 minutes. Then, 2 g of MAX powder was incrementally added to this etching solution. This mixture was placed in a rotating heating bath at 40°C for 24 hours. Subsequent steps involved multiple washings with deionized water and centrifugation at 4200 rpm until the pH exceeded 7. The resultant mixture was vacuum-filtered to form a film, which was then dispersed in 200 ml of deionized water and sonicated for 1 hour in an ice bath under an argon atmosphere. Following sonication, the mixture was centrifuged for 1 hour to yield multilayer $Ti_3C_2T_x$, which was then poured into petri dishes and dried in vacuum oven at 80°C for 12 hours. The etching reactions take place according to following equations;

$$HCl + LiF \rightarrow HF + LiCl ----- Eq\ S2$$

$$Ti_3AlC_2 + 6HF \rightarrow 3Ti_3C_2 + 3AlF_3 + 3H_2 ------ Eq\ S3$$

S1.3. Synthesis of ZnSe@$Ti_3C_2T_x$ nanocomposite:

The CTAB-modified ZnSe spheres, with enhanced dispersion and surface charge modification, facilitate the efficient incorporation of $Ti_3C_2T_x$ layers. The ZnSe spheres and $Ti_3C_2T_x$ were mixed in a 1:3 ratio with polyvinyl ethylene glycol as a dispersant. After stirring for 30 minutes, the mixture was autoclaved at 180°C for 12 hours and cooled at a rate of 1°C per minute. The resultant product was filtered, washed with deionized water and ethanol, and oven-dried at 60°C for 4 hours.

S1.4. Electrode synthesis for electrochemical evaluation by SEM images:

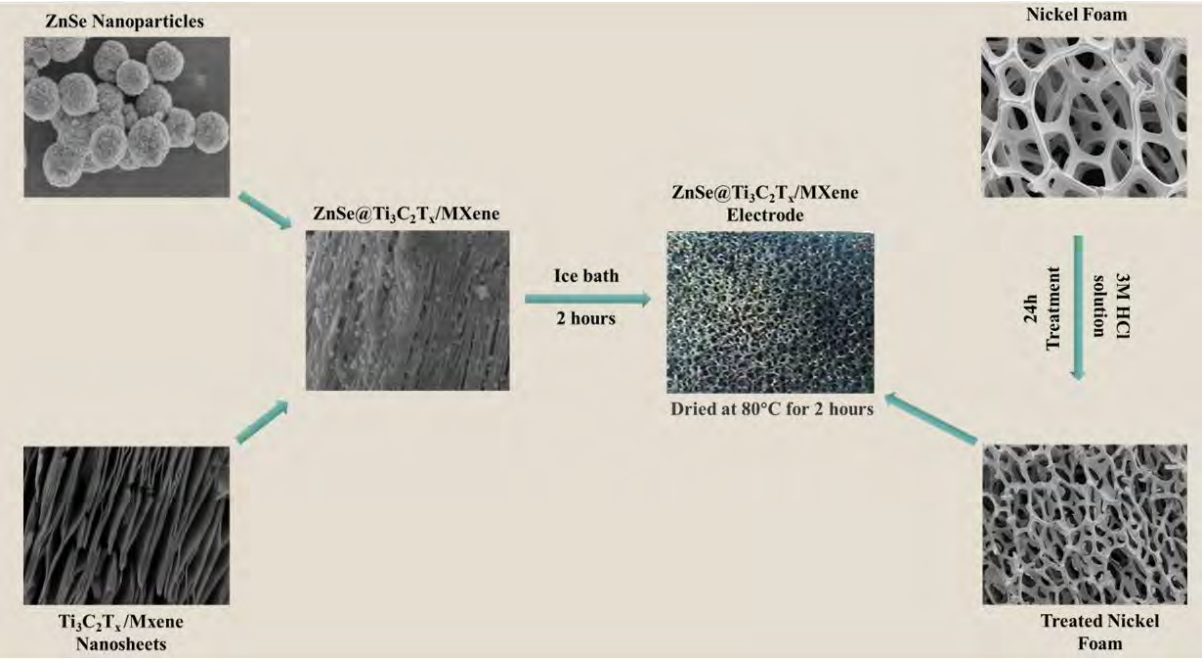

Fig. S 1 $ZnSe@Ti_3C_2T_x$ electrode synthesis illustrated by SEM images.

S2. Characterizations and computation:

Following the successful synthesis of $Ti_3C_2T_x$, ZnSe, and $ZnSe@Ti_3C_2T_x$, a comprehensive suite of advanced characterization techniques was applied to investigate their materialistic properties. Morphological analysis was conducted using field emission scanning electron microscopy (FE-SEM, Hitachi S4800, Japan) and high-resolution transmission electron microscopy (HRTEM, JEOL JEM-2000 FX). Elemental composition and surface analysis were performed through energy-dispersive X-ray spectroscopy (EDS, JEM 2100F, JEOL, Tokyo, Japan). The crystalline structures of the materials were identified via X-ray diffraction (XRD, D/MAX-2250VB+/PC, Rigaku, Tokyo, Japan), employing a Philips diffractometer with X' PertPro monochromatized Cu Kα radiation (λ=1.54 Å). Raman spectroscopy and UV-visible diffuse reflectance spectroscopy (UV-Vis DRS, PerkinElmer Lambda 35) provided insights into vibrational modes, light absorption, and band gap energies. X-ray photoelectron spectroscopy (XPS, ESCALAB 250XI, Thermo Fisher, Waltham, USA) elucidated the

nanoparticles' structural and optical characteristics. Density-functional theory (DFT) is also performed to study the electrochemical properties of the ZnSe@$Ti_3C_2T_x$ composite by using the Vienna ab initio simulation package (VASP) [1,2]. The project-augmented-wave (PAW) [3] method and the Perdew-Burke-Ernzerhof (PBE) generalized gradient approximation (GGA) [4] method was employed for handling pseudopotentials and exchange correlation functionals, respectively. To ensure accurate results, a plane wave cutoff of 520 eV was applied to the kinetic energy, and all self-consistent field computations converged with a criterion of 1×10-5 eV. To evaluate the adsorption energies of ZnSe, $Ti_3C_2T_x$ and ZnSe@ $Ti_3C_2T_x$, three distinct computational models in the form of rectangular parallelepipeds were constructed. These models had dimensions of 8.5 Å × 4.9 Å × 25 Å and consisted of ZnSe, $Ti_3C_2T_x$, and ZnSe composite with $Ti_3C_2T_x$, respectively. The ZnSe layer had a thickness of 5.3 Å. To prevent interactions between adjacent periodic images, a vacuum layer of 15 Å was introduced along the z-axis to separate each model effectively. The integration of the Brillouin zone was performed using a Monkhorst-Pack [5] k-mesh of 4 × 7 × 1, which ensured proper resolution for the calculations while maintaining computational efficiency. By employing these computational methods and models, a comprehensive understanding of the electrochemical properties and adsorption energies of the ZnSe@$Ti_3C_2T_x$ composite and its constituent materials was achieved. In addition to the DFT calculations, the Gibbs free energy for hydrogen (H) and water (H_2O) adsorption was also evaluated. The Gibbs free energy (ΔG) provides insight into the interaction strength between adsorbates and the composite surface, which is critical for understanding catalytic activity. A more negative ΔG for H adsorption indicates a stronger interaction, beneficial for enhancing hydrogen evolution reaction (HER) kinetics, while ΔG for water adsorption reflects the composite's role in the oxygen evolution reaction (OER) process.

S.3 SEM and TEM and HRTEM Images of Synthesized samples:

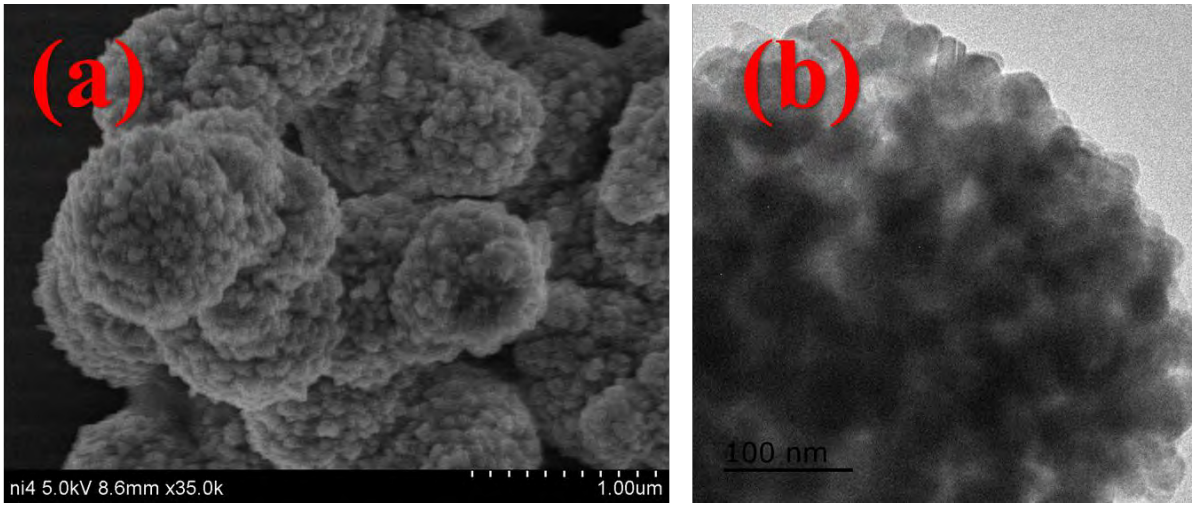

Fig. S 2 images of ZnSe, (a) SEM (b) TEM

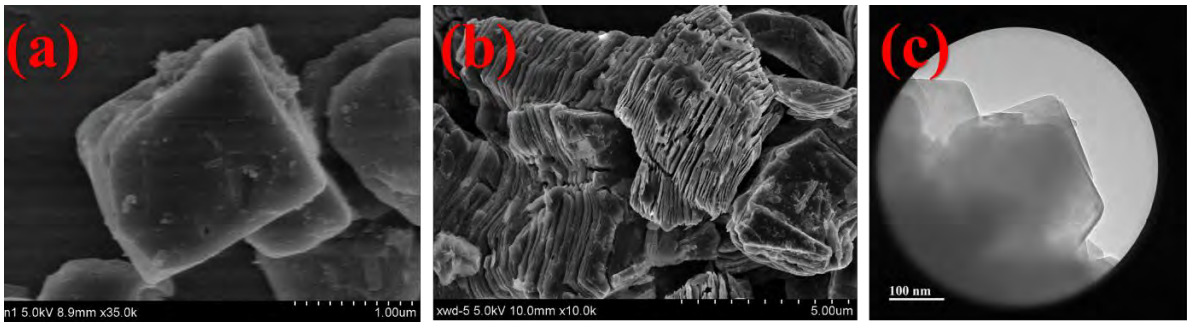

Fig. S 3 SEM images of (a) Ti_3AlC_2 (b) $Ti_3C_2T_x$; (c) HRTEM image of $Ti_3C_2T_x$.

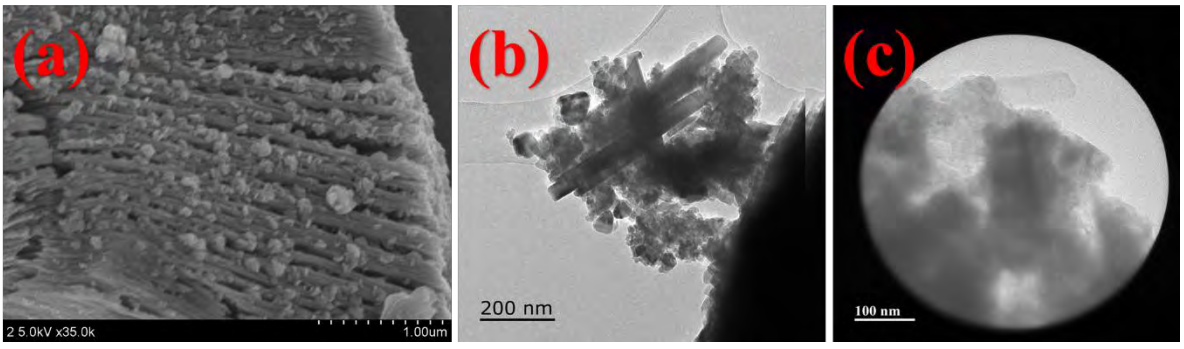

Fig. S 4. images of ZnSe@$Ti_3C_2T_x$, (a) SEM (b) TEM (c) HRTEM.

S.4 BET:

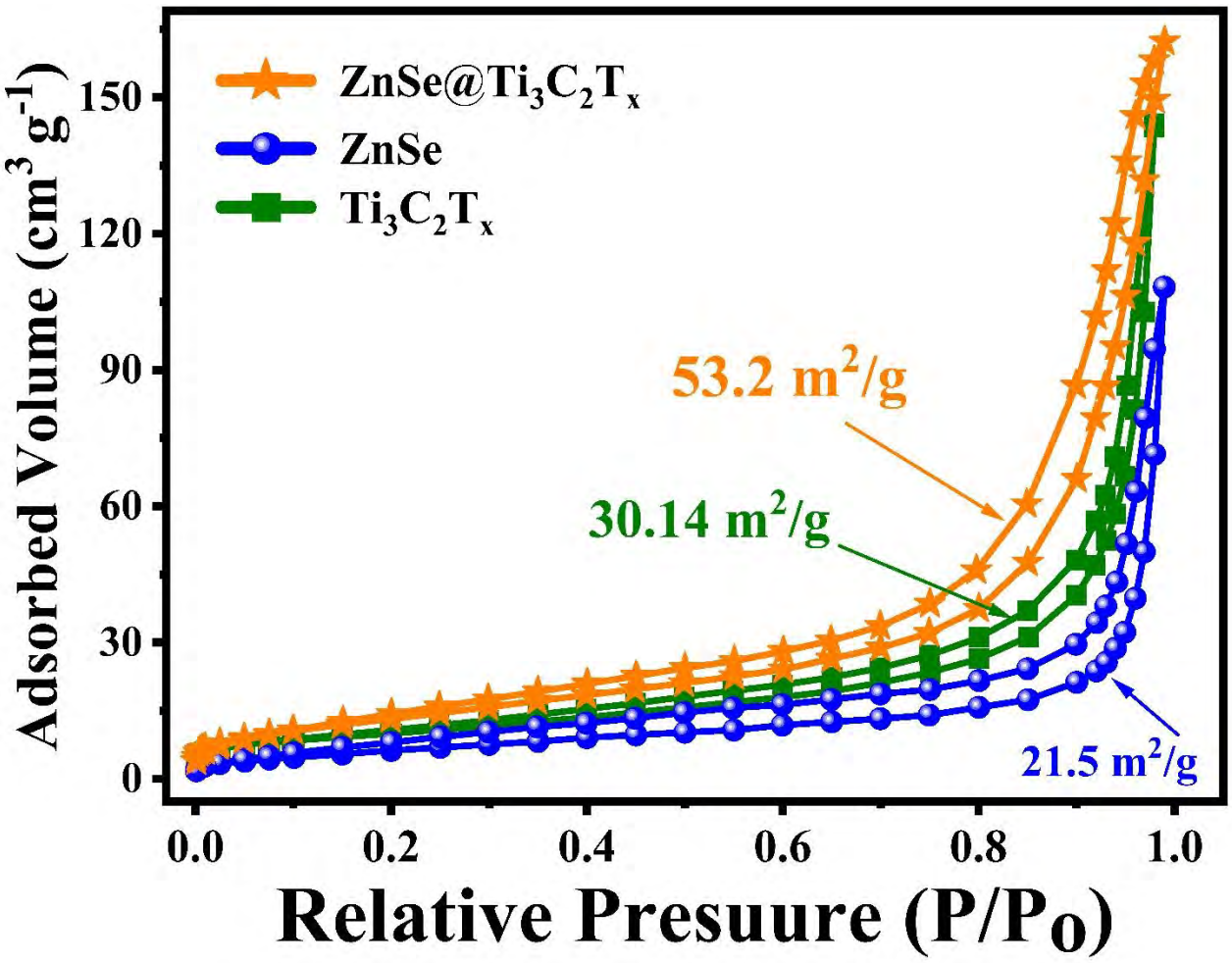

Fig S 5. BET analysis of synthesized materials.

S.5 Electrochemical measurements:

The CHI660E electrochemical workstation was employed to perform the three-electrode evaluation in 1 M KOH. Three-electrode setup was used for that purpose: a) $Hg/Hg_2Cl_2/KCl$ served as the reference electrode with a potential of 0.238 V, b) A Pt wire was utilized as the counter electrode, c) The working electrode completed the setup where Nickel foam, $Ti_3C_2T_x$, ZnSe and ZnSe@$Ti_3C_2T_x$ was used as working electrode and mass loading was set at 2.86 mg cm^{-2}. The electrochemical properties of the electrodes were assessed through cyclic voltammetry (CV), galvanostatic charge-discharge (GCD) analysis, and electrochemical impedance spectroscopy (EIS). Furthermore, the electrolysis properties were investigated through linear sweep voltammetry (LSV), Tafel slopes, Over Potentials and chronoamperometry test.

Current measurements were taken across the counter and working electrodes while potential was applied between the reference and counter electrodes. The potential window was set between 0 V to 0.6 V, while the scan rate was varied between 1 to 150 mV s^{-1}. Electrochemical impedance spectra (EIS) of synthesized sample were determined in the frequency range of 100 k Hz to 0.1 Hz at 5 mV amplitude.

To assess the electrochemical properties of energy storage Asymmetric supercapacitor CV and GCD test were performed at different scan rate to calculate the electrochemical and Pseudocapacitive behaviour of electrode. Specific capacitance (C_m, F g^{-1}), power density (P, W kg^{-1}) and Energy density (E, Wh kg^{-1}) values were also calculated to relate different parameters by using Eq. (1), (2) and (3) given bellow.

$$C_m = \frac{I \times \Delta t}{m \times \Delta V} \ (\mathrm{F}\ g^{-1}) - - - - - Eq\ S4$$

Here Δt is discharging period, I indicating galvanostatic discharging current, ΔV was used for discharging voltage window, m indicates mass of electrode.

$$E = \frac{C_m(\Delta V)^2}{2} \times \frac{1000}{3600}\ (\text{Wh}\ kg^{-1}) - - - -\text{Eq S5}$$

$$P = \frac{3600 \times E}{\Delta t}\ (\text{W}\ kg^{-1}) - - - - - Eq\ S6$$

Here ΔV for voltage window (V), E for energy density and P for Power Density.

The OER (oxygen evolution reaction) and HER (hydrogen evolution reaction) were investigated using Linear Sweep Voltammetry (LSV). The potential window for the OER was fixed at 0 to 1.6 V, while for the HER, it was fixed at 0 to -2 V. The Tafel slope was also determined by analysing the linear portion of the Tafel plot. To calculate the overpotential (η), the experimental potential values were subtracted from the standard potential for water oxidation (1.23 V) using the following equation:

$$\eta = V(vs.RHE) - 1.23\ V - - - - - Eq\ S7$$

S5.1. CV and GCD N.F & $Ti_3C_2T_x$:

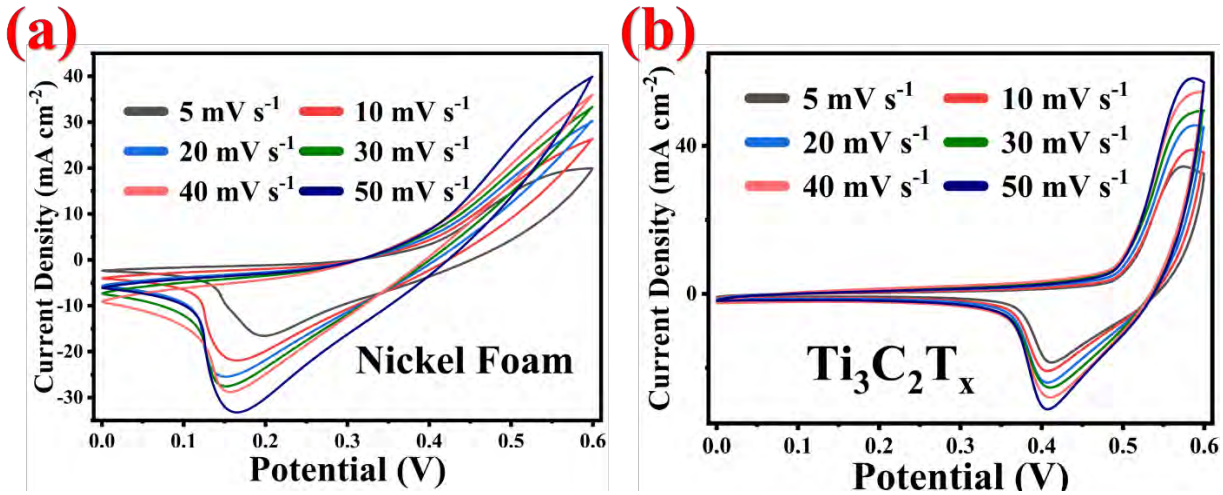

Fig. S 6. CV curves of (a) Nickel Foam, (b) $Ti_3C_2T_x$.

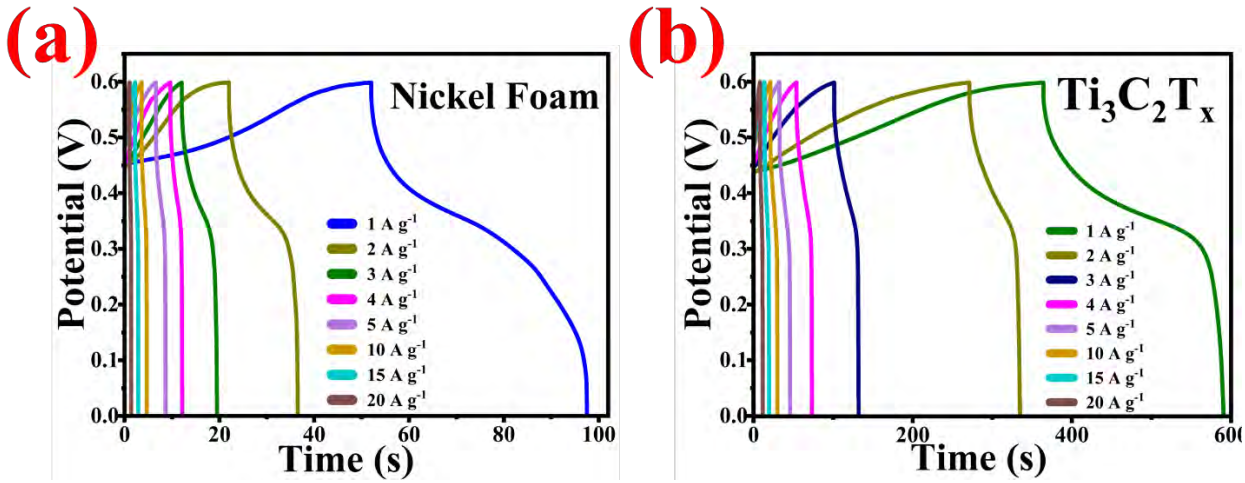

Fig. S 7. GCD of (a) Nickel Foam, (b) $Ti_3C_2T_x$.

S.5.2. Bode Plot for EIS:

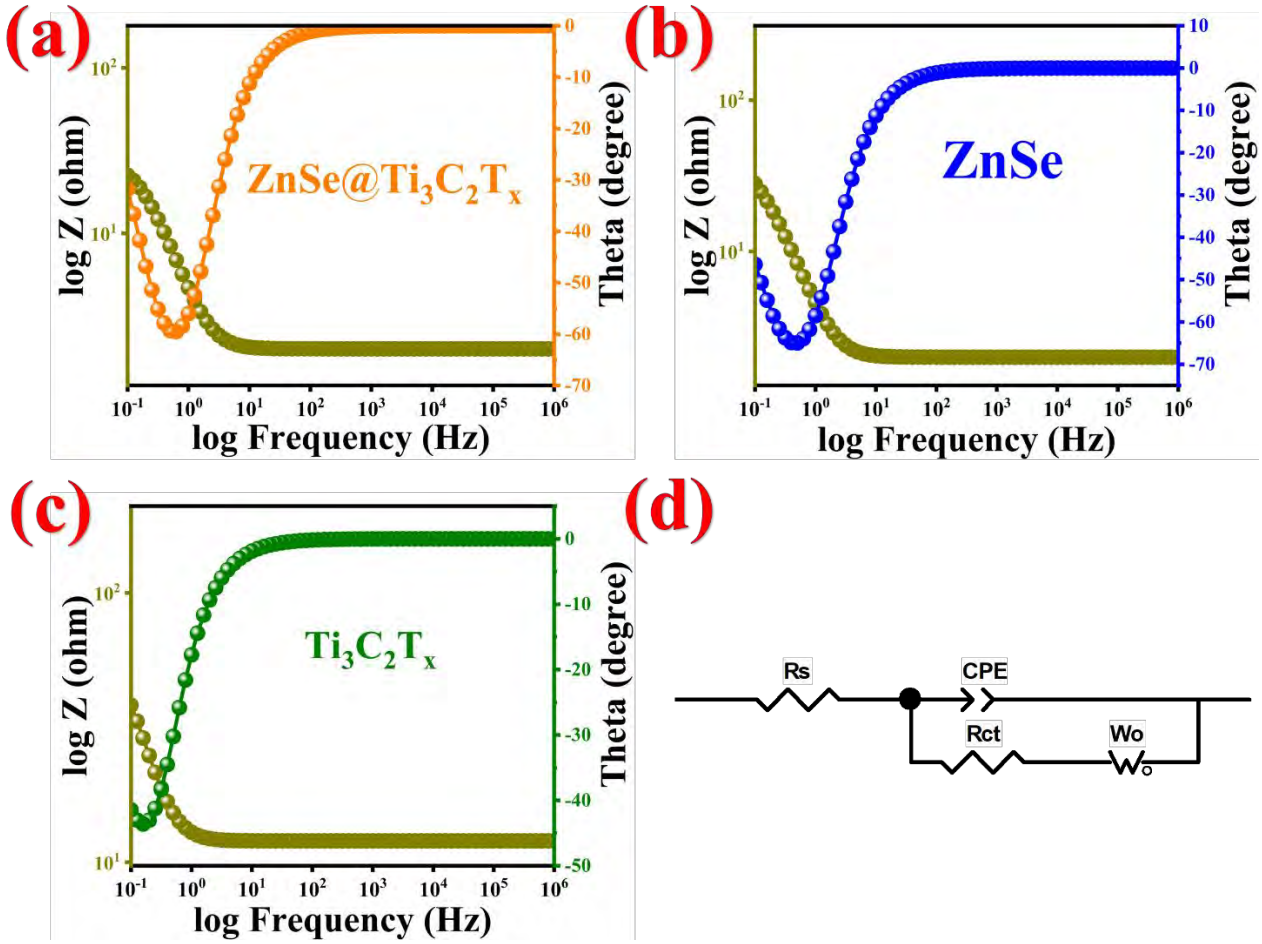

Fig. S 8 Bode plot of (a) ZnSe@$Ti_3C_2T_x$ (b)$Ti_3C_2T_x$ (c) ZnSe.

Table S 1. Equivalent Resistance for electrodes.

Electrodes	**R_s**	**R_{ct}**	**R_w**
ZnSe@$Ti_3C_2T_x$	2	25	0.25
ZnSe	4	37	0.18
$Ti_3C_2T_x$	12	48	0.7

S.5.3. CV & GCD graphs for AC:

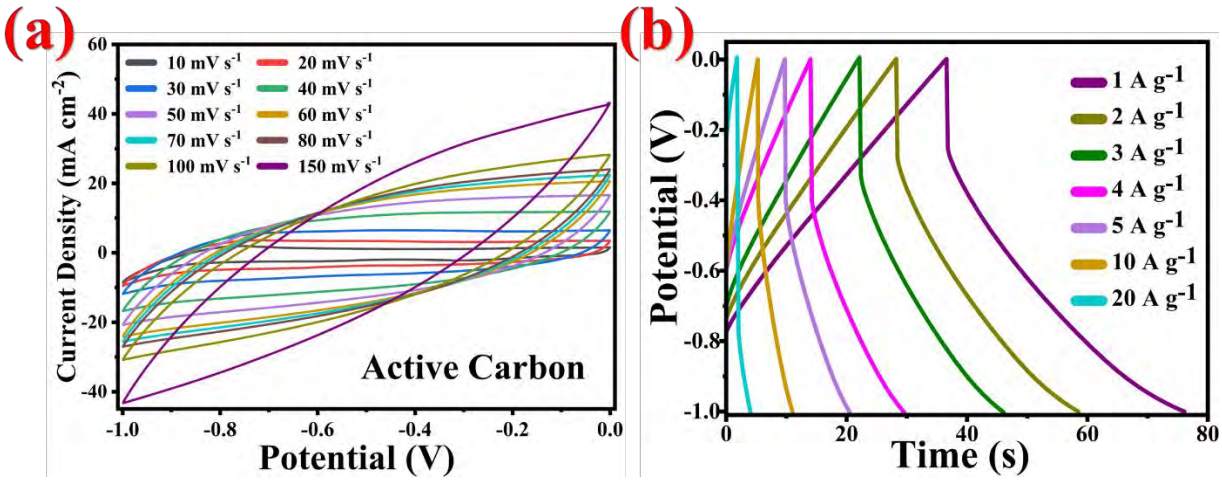

Fig. S 9. CV and GCD curves for AC (a) CV (b) GCD.

S.5.4: Bode plot of ZnSe@$Ti_3C_2T_x$//AC-APSC:

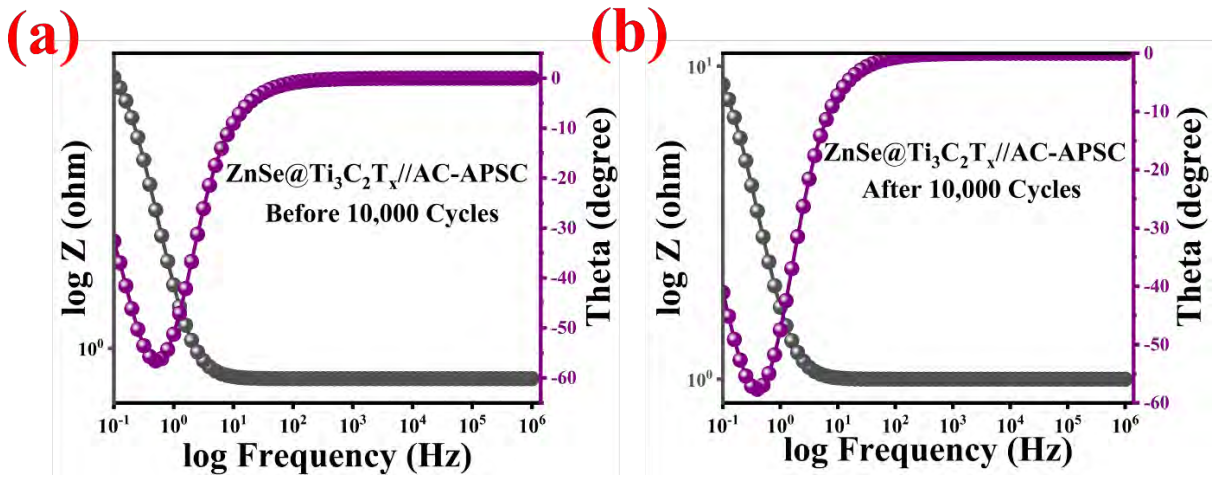

Fig. S 10. Bode plot of ZnSe@$Ti_3C_2T_x$//AC-APSC (a) before 10,000 GCD cycles (b) After 10,000 GCD cycles.

Table S 2. Equivalent resistance of before and after cyclic stability.

State	R_s	R_{ct}	R_w
Before 10k cycles	0.8	8	0.36
After 10k cycles	1	10.55	0.47

S. 5.5: Practical Application of AC//ZnSe@$Ti_3C_2T_x$-APSC

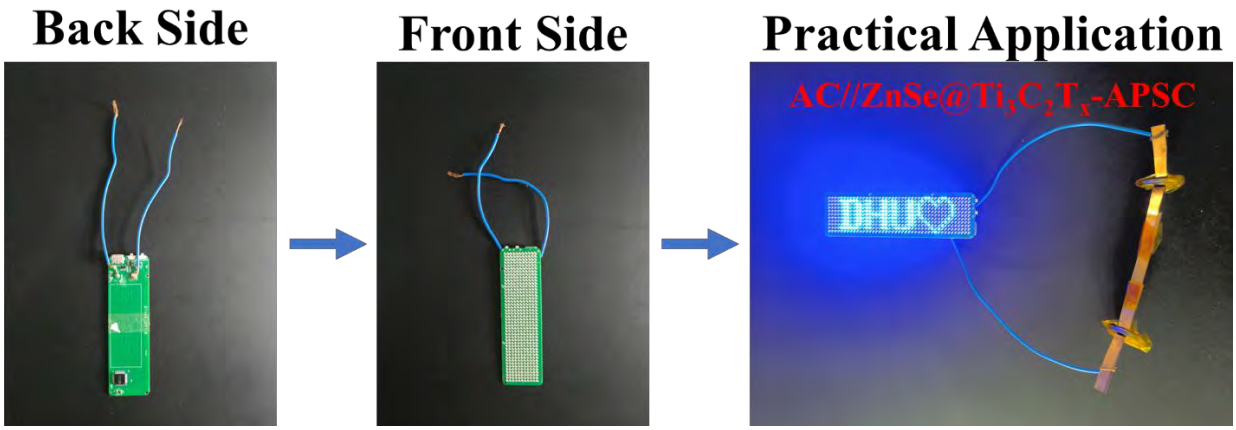

Fig. S 5. The practical application involves the utilization of two AC//ZnSe@Ti3C2Tx-APSC devices connected in a series circuit to illuminate light-emitting diodes (LEDs) arranged to form the inscription "DHU ♡"

S6. Electrochemical Water-splitting:

Water electrolysis produces hydrogen (H_2) and oxygen (O_2) on the cathode and anode accompanied with oxygen evolution reaction (OER) and hydrogen evolution reaction (HER) , respectively. The electrodes for water electrolysis were prepared with the same process as described earlier. All experimental tests were conducted in a 1 M potassium hydroxide (KOH) electrolyte solution.

S6.1 OER:

In the present investigation, a comprehensive examination of the Oxygen Evolution Reaction (OER) was conducted, focusing on meticulous analysis. ZnSe@$Ti_3C_2T_x$, recognized for its exceptional properties, was employed as the anode material. The cathode consisted of a Pt wire, while the renowned Hg/Hg_2Cl_2 configuration served as the reference electrode. During the OER process, an intriguing phenomenon was observed, whereby hydroxide ions (OH^-) adsorbed onto the electrode surface, initiating a cascade of chemical reactions. At the interface between the electrode and the electrolyte, a four-electron transfer process transpired, resulting in the liberation of oxygen gas (O_2) and water molecules (H_2O). The purpose of these experimental tests was to unravel the underlying mechanism of the OER and explore its potential applications in the field of water splitting technologies.

S6.2. HER:

In the current investigation, the cathode material chosen for the Hydrogen Evolution Reaction (HER) was ZnSe@$Ti_3C_2T_x$. The anode material was a Pt wire, and the reference electrode used was Hg/Hg_2Cl_2. In the process of HER, protons (H^+) are adsorbed onto the surface of the

electrode. This is followed by a Tafel reaction at the interface between the electrode and the electrolyte, resulting in the generation of hydrogen gas (H_2).

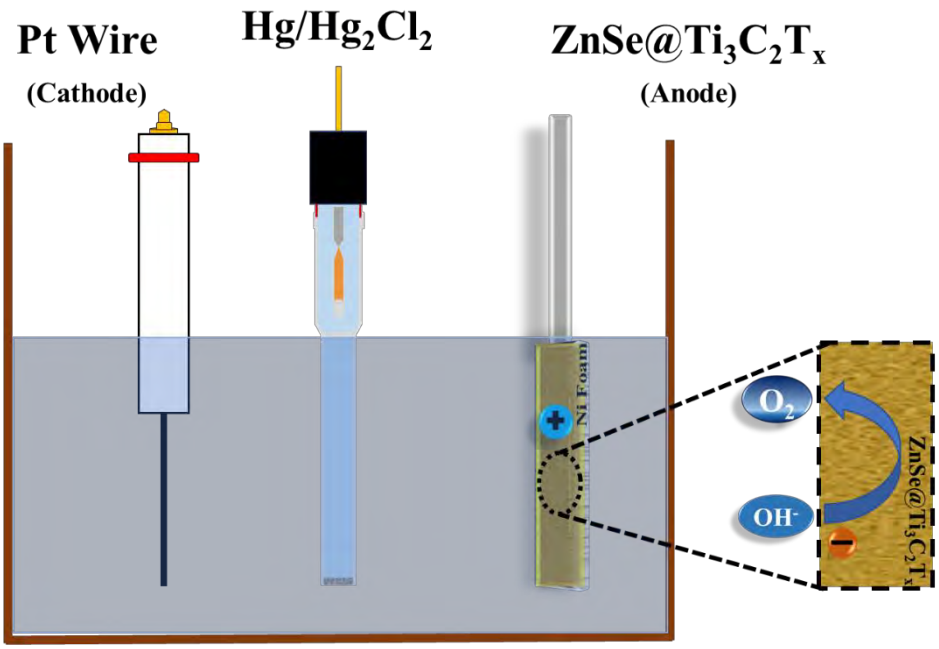

Fig. S 6 illustrate OER by using ZnSe@$Ti_3C_2T_x$ electrode.

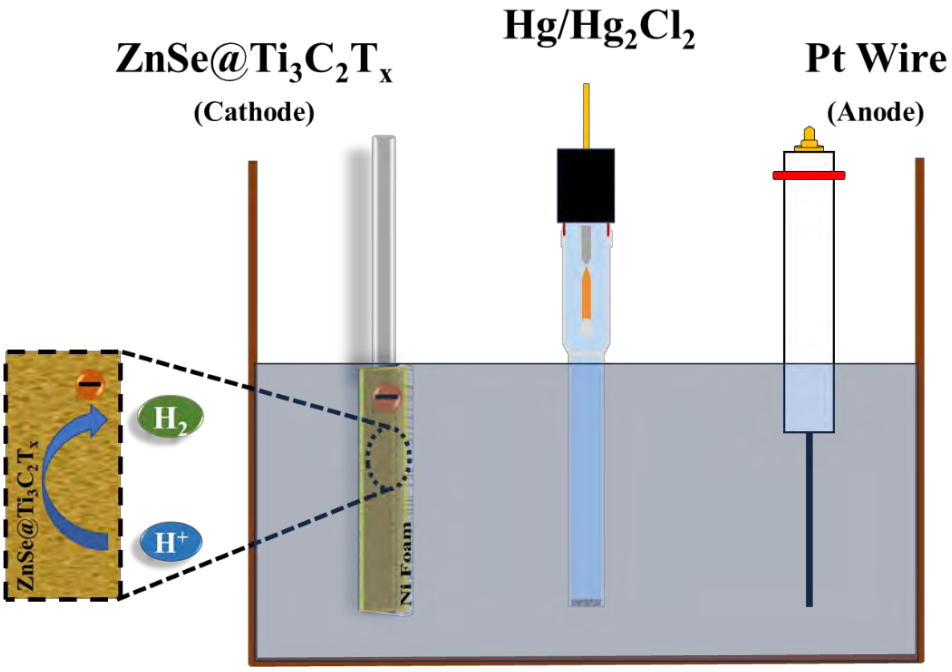

Fig. S 7 illustrate HER by using $ZnSe@Ti_3C_2T_x$ electrode.

S5.1. Chronoamperometry test for ZnSe, $Ti_3C_2T_x$:

Chronoamperometry tests reveal that ZnSe can endure in alkaline media (7M KOH) for approximately 8.52 hours, but its current density exhibits instability over time. In contrast, MXene can only sustain a stable current density for about 5.15 hours, with a gradual and continuous decline in its current density. The limited stability of both ZnSe and $Ti_3C_2T_x$ in the alkaline solution can be attributed to surface degradation and electrochemical instability under harsh conditions. However, when tested in the same solution, the ZnSe@$Ti_3C_2T_x$ composite maintains a stable current density for over 10 hours, indicating the protective effect of the MXene layer. This enhanced stability can be attributed to the synergistic interaction between ZnSe and $Ti_3C_2T_x$, which prevents the degradation of ZnSe and mitigates the electrochemical instability of $Ti_3C_2T_x$, thereby improving the overall performance of the composite.

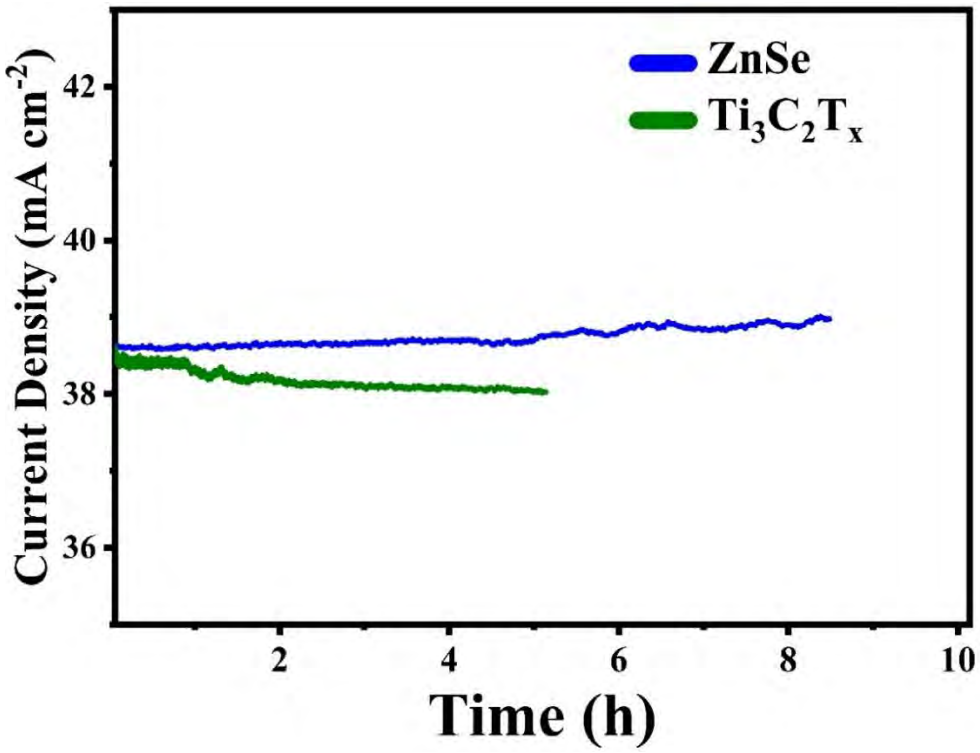

Fig S 14. Chronoamperometry Test for ZnSe and $Ti_3C_2T_x$.

S7. Electrochemical behaviour of MXene-based electrodes for supercapacitors:

Table S 3. Electrochemical properties of $Ti_3C_2T_x$/MXene based electrode that are previously reported.

MXene based devices	**Electrolyte**	**Potential window (V)**	**Specific capacitance**	**Current Density mA cm^{-2}**	**Energy density (Wh kg^{-1})**	**Power density (W kg^{-1})**	**Capacitance retention (%)**	**Number of cycles**	**Ref.**
AC//ZnSe@$Ti_3C_2T_x$/MXene	**7 M KOH**	**1.6**	**259.1 F g^{-1}**	**1 A g^{-1}**	**92.9**	**1000**	**91.92**	**10000**	**This Work**
rGO//$Ti_3C_2T_x$	3 M H_2SO_4	1.8	76.5 F g^{-1}	1 A g^{-1}	34.4	1000	~100	10000	6
NiCo-MOF/$Ti_3C_2T_x$/AC	2 M KOH	1.5	126.4 F g^{-1}	0.5 A g^{-1}	39.5	562.5	82.3	10000	7
$NiCo_2S_4$/MXene//AC	KOH	1.7	171.2	1 A g^{-1}	68.7	850	89.5	5000	8

MXene/NCF//MXene/NCF	PVA/KOH	1.0	63 F g^{-1}	1 A g^{-1}	8.75	1871	96	2500	9
$Ti_3C_2T_x$/$CuCo_2S_4$//AC	6 M KOH	1.6	269.4 C g^{-1}	1 A g^{-1}	66.8	895.1	88.2	10000	10
rGO/CNT/PANI//$Ti_3C_2T_x$	3 M H_2SO_4	1.5	116.9	10 mV s^{-1}	28.6	590	80	10000	11
RuO_2//$Ti_3C_2T_x$	PVA-H_2SO_4	1.6	93 F g^{-1}	50 mV s^{-1}	29	3800	86	20000	12
$Ti_3C_2T_x$/NiS//G/AC	2 M KOH	1.5	56.73	1 A g^{-1}	17.69	750	97.7	3000	13
$MnCo_2S_4$/MXene//AC	3 M KOH	1.6	460 C g^{-1}	0.5 A g^{-1}	25.6	6400	100	12000	14
NiFe-LDH/$Ti_3C_2T_x$//AC	1 M KOH	1.3	135.7 F g^{-1}	1 A g^{-1}	42.4	758.27	86	1000	15

S7. OER performance of Electrocatalysts:

Table S 4. OER behaviour of $Ti_3C_2T_x$/MXene based electrocatalysts.

Electrocatalyst	**Electrolyte**	**Over Potential (mV)**	**Tafel Slope ($mV\ dec^{-1}$)**	**Ref.**
ZnSe@$Ti_3C_2T_x$/MXene	**1M KOH**	**185**	**51**	**This Work**
N-$CoSe_2$/3D $Ti_3C_2T_x$	0.1 M KOH	310	45.0	16
1T/2H $MoSe_2$/MXene	1.0 M KOH	340	90.0	17
FeNi-LDH/Ti_3C_2	1.0 M KOH	298	43.0	18
Co-LDH@$Ti_3C_2T_x$	1.0 M KOH	330	82.0	19
CoP/MXene	1.0 M KOH	230	50.0	20

S8. HER performance of Electrocatalysts:

Table S 5. HER behaviour of several $Ti_3C_2T_x$/MXene based electrocatalysts reported previously along with the comparison of this work.

Electrocatalyst	**Electrolyte**	**Over Potential (mV)**	**Tafel Slope ($mV\ dec^{-1}$)**	**Ref.**
ZnSe@$Ti_3C_2T_x$/MXene	**1M KOH**	96	36	**This Work**
$MoSe_2$/MXene-O	0.5 M H_2SO_4	171	61	21
$NiSe_2$/Ti3C2Tx	0.5 M H_2SO_4	200	37.7	22
NiFe-LDH/Ti3C2Tx	1.0 M KOH	132	70	23
Co-MoS_2/Mo_2CT_x	1.0 M KOH	112	82	24

References:

1. Wang, Kaifeng, Yujie Chen, Ran Tian, Hua Li, Ying Zhou, Huanan Duan, and Hezhou Liu., Porous Co–C core–shell nanocomposites derived from Co-MOF-74 with enhanced electromagnetic wave absorption performance, ACS applied materials & interfaces. 10, 13 (2018) 11333-11342. https://doi.org/10.1021/acsami.8b00965
2. Kresse, Georg, and Jürgen Furthmüller., Efficiency of ab-initio total energy calculations for metals and semiconductors using a plane-wave basis set, Computational materials science. 6 1 (1996) 15-50. https://doi.org/10.1016/0927-0256(96)00008-0
3. Kresse, Georg, and Jürgen Furthmüller., Efficient iterative schemes for ab initio total-energy calculations using a plane-wave basis set, Physical review B 54, 16 (1996) 11169. https://doi.org/10.1103/PhysRevB.54.11169
4. Kresse, Georg, and Daniel Joubert., From ultrasoft pseudopotentials to the projector augmented-wave method, Physical review b. 59, 3 (1999) 1758. https://doi.org/10.1103/PhysRevB.59.1758
5. Perdew, John P., Kieron Burke, and Matthias Ernzerhof., Generalized gradient approximation made simple., Physical review letters. 77, 18 (1996) 3865. https://doi.org/10.1103/PhysRevLett.77.3865
6. Li, Mai, Zheyi Meng, Ruichao Feng, Kailan Zhu, Fengfeng Zhao, Chunrui Wang, Jiale Wang, Lianwei Wang, and Paul K. Chu., Fabrication of bimetallic oxides (MCo2O4: M= Cu, Mn) on ordered microchannel electro-conductive plate for high-performance hybrid supercapacitors, Sustainability 13. 17 (2021) 9896. https://doi.org/10.3390/su13179896
7. Wang, Yanzhong, Yuexin Liu, Chao Wang, Hu Liu, Jiaoxia Zhang, Jing Lin, Jincheng Fan, Tao Ding, Jong E. Ryu, and Zhanhu Guo., Significantly enhanced ultrathin NiCo-based MOF nanosheet electrodes hybrided with Ti3C2Tx MXene for high performance

asymmetric supercapacitor, Engineered Science 9. 12 (2020) 50-59. http://dx.doi.org/10.30919/es8d903

8. Fu, Jianjian, Lei Li, Je Moon Yun, Damin Lee, Bong Ki Ryu, and Kwang Ho Kim., Two-dimensional titanium carbide (MXene)-wrapped sisal-Like NiCo2S4 as positive electrode for High-performance hybrid pouch-type asymmetric supercapacitor, Chemical Engineering Journal. 375 (2019) 121939. https://doi.org/10.1016/j.cej.2019.121939
9. Sun, Li, Gongsheng Song, Yafei Sun, Qiang Fu, and Chunxu Pan., MXene/N-doped carbon foam with three-dimensional hollow neuron-like architecture for freestanding, highly compressible all solid-state supercapacitors, ACS Applied Materials & Interfaces. 12, 40 (2020) 44777-44788. https://doi.org/10.1021/acsami.0c13059
10. X. Chen, Z. Ding, H. Yu, H. Ge, W. Liu, S. Sun, Facile fabrication of CuCo2S4 nanoparticles/MXene composite as anode for high-performance asymmetric supercapacitor. Mater. Chem. Front. 5 (2021) 7606-7616. https://doi.org/10.1039/D1QM01029H
11. Li, Ke, Xuehang Wang, Xiaofeng Wang, Meiying Liang, Valeria Nicolosi, Yuxi Xu, and Yury Gogotsi., All-pseudocapacitive asymmetric MXene-carbon-conducting polymer supercapacitors, Nano Energy. 75 (2020) 104971. https://doi.org/10.1016/j.nanoen.2020.104971
12. Jiang, Qiu, Narendra Kurra, Mohamed Alhabeb, Yury Gogotsi, and Husam N. Alshareef., All pseudocapacitive MXene-RuO2 asymmetric supercapacitors, Advanced Energy Materials. 8 13 (2018) 1703043. https://doi.org/10.1002/aenm.201703043
13. Liu, Hao, Rui Hu, Jiqiu Qi, Yanwei Sui, Yezeng He, Qingkun Meng, Fuxiang Wei, Yaojian Ren, and Yulong Zhao., A facile method for synthesizing NiS nanoflower grown on MXene (Ti3C2Tx) as positive electrodes for “supercapattery”, Electrochimica Acta. 353 (2020) 136526. https://doi.org/10.1016/j.electacta.2020.136526

14. Nasrin, K., K. Subramani, M. Karnan, and M. Sathish., MnCo2S4–MXene: A novel hybrid electrode material for high performance long-life asymmetric supercapattery, Journal of Colloid and Interface Science. 600 (2021) 264-277. https://doi.org/10.1016/j.jcis.2021.05.037
15. H. Zhou, F. Wu, L. Fang, J. Hu, H. Luo, T. Guan, B. Hu, M. Zhou., Layered NiFe-LDH/MXene nanocomposite electrode for high-performance supercapacitor, Int. J. Hydrog. Energy. 45 (2020) 13080-13089. https://doi.org/10.1016/j.jcis.2021.05.037
16. Zeng, Zhiping, Gengtao Fu, Hong Bin Yang, Yibo Yan, Jie Chen, Zhongzheng Yu, Jiajian Gao, Li Yong Gan, Bin Liu, and Peng Chen., Bifunctional N-CoSe2/3D-MXene as highly efficient and durable cathode for rechargeable Zn–air battery, ACS Materials Letters 1, 4 (2019) 432-439. https://doi.org/10.1021/acsmaterialslett.9b00337
17. Li, Nan, Yifan Zhang, Meilin Jia, Xinding Lv, Xitao Li, Ran Li, Xiaoqing Ding, Yan-Zhen Zheng, and Xia Tao., 1T/2H MoSe2-on-MXene heterostructure as bifunctional electrocatalyst for efficient overall water splitting, Electrochimica Acta. 326 (2019) 134976. https://doi.org/10.1016/j.electacta.2019.134976
18. Yu, Mengzhou, Si Zhou, Zhiyu Wang, Jijun Zhao, and Jieshan Qiu., Boosting electrocatalytic oxygen evolution by synergistically coupling layered double hydroxide with MXene, Nano Energy. 44 (2018) 181-190. https://doi.org/10.1016/j.nanoen.2017.12.003
19. Benchakar, Mohamed, Thomas Bilyk, Cyril Garnero, Lola Loupias, Claudia Morais, Jérôme Pacaud, Christine Canaff et al., MXene supported cobalt layered double hydroxide nanocrystals: facile synthesis route for a synergistic oxygen evolution reaction electrocatalyst, Advanced Materials Interfaces. 6 23 (2019) 1901328. https://doi.org/10.1002/admi.201901328

20. Benchakar, Mohamed, Thomas Bilyk, Cyril Garnero, Lola Loupias, Claudia Morais, Jérôme Pacaud, Christine Canaff et al., MXene supported cobalt layered double hydroxide nanocrystals: facile synthesis route for a synergistic oxygen evolution reaction electrocatalyst, Advanced Materials Interfaces. 6 23 (2019) 1901328. https://doi.org/10.1002/admi.201901328
21. Xiao, Weiping, Daqiang Yan, Yu Zhang, Xiaofei Yang, and Tierui Zhang., Heterostructured MoSe2/oxygen-terminated Ti3C2 MXene architectures for efficient electrocatalytic hydrogen evolution, Energy & Fuels. 35 5 (2021) 4609-4615. https://doi.org/10.1021/acs.energyfuels.1c00123
22. Jiang, Hanmei, Zegao Wang, Qian Yang, Luxi Tan, Lichun Dong, and Mingdong Dong., Ultrathin Ti 3 C 2 T x (MXene) nanosheet-wrapped NiSe 2 octahedral crystal for enhanced supercapacitor performance and synergetic electrocatalytic water splitting, Nano-Micro Letters 11 (2019) 1-14. https://doi.org/10.1007/s40820-019-0261-5
23. Yu, Mengzhou, Zhiyu Wang, Junshan Liu, Fu Sun, Pengju Yang, and Jieshan Qiu., A hierarchically porous and hydrophilic 3D nickel–iron/MXene electrode for accelerating oxygen and hydrogen evolution at high current densities, Nano Energy. 63 (2019) 103880. https://doi.org/10.1016/j.nanoen.2019.103880
24. Liang, Junmei, Chaoying Ding, Jiapeng Liu, Tao Chen, WenChao Peng, Yang Li, Fengbao Zhang, and Xiaobin Fan., Heterostructure engineering of Co-doped MoS 2 coupled with Mo 2 CT x MXene for enhanced hydrogen evolution in alkaline media, Nanoscale. 11 22 (2019) 10992-11000. https://doi.org/10.1039/C9NR02085C